

Structure-Guided Design of Potent Inhibitors of SARS-CoV-2 3CL Protease: Structural, Biochemical, and Cell-Based Studies

Chamandi S. Dampalla,[#] Athri D. Rathnayake,[#] Krishani Dinali Perera, Abdul-Rahman M. Jesri, Harry Nhat Nguyen, Matthew J. Miller, Hayden A. Thurman, Jian Zheng, Maithri M. Kashipathy, Kevin P. Battaile, Scott Lovell, Stanley Perlman, Yunjeong Kim,^{*} William C. Groutas,^{*} and Kyeong-Ok Chang^{*}



Cite This: <https://doi.org/10.1021/acs.jmedchem.1c01037>



Read Online

ACCESS |



Metrics & More

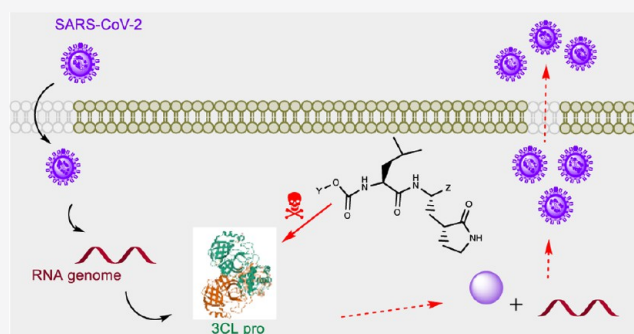


Article Recommendations



Supporting Information

ABSTRACT: The COVID-19 pandemic is having a major impact on public health worldwide, and there is an urgent need for the creation of an armamentarium of effective therapeutics, including vaccines, biologics, and small-molecule therapeutics, to combat SARS-CoV-2 and emerging variants. Inspection of the virus life cycle reveals multiple viral- and host-based choke points that can be exploited to combat the virus. SARS-CoV-2 3C-like protease (3CLpro), an enzyme essential for viral replication, is an attractive target for therapeutic intervention, and the design of inhibitors of the protease may lead to the emergence of effective SARS-CoV-2-specific antivirals. We describe herein the results of our studies related to the application of X-ray crystallography, the Thorpe–Ingold effect, deuteration, and stereochemistry in the design of highly potent and nontoxic inhibitors of SARS-CoV-2 3CLpro.



INTRODUCTION

Severe acute respiratory syndrome coronavirus 2 (SARS-CoV-2) is the etiological agent of coronavirus disease (COVID-19).¹ The severity of the ongoing pandemic is having a major impact on public health worldwide and is further exacerbated by the emergence of more virulent strains.^{2,3} Intense worldwide efforts to combat the virus have led to the successful development of FDA-approved vaccines, and an array of potential therapeutics, such as monoclonal antibodies, repurposed drugs, and others, are currently being evaluated in clinical trials or are at various stages of clinical development.^{4,5}

The SARS-CoV-2 life cycle encompasses multiple viral- and host-based druggable targets that can be exploited, including, for example, inhibitors that block virus entry and fusion, and replication inhibitors targeting the 3C-like protease (3CLpro), papain-like protease and the RNA-dependent RNA polymerase, among others. Attractive host-based targets include the proteases transmembrane serine protease 2 (TMPRSS2), cathepsin L, and furin. Thus, the development of small-molecule therapeutics that target host or viral targets essential for viral replication is a potentially fruitful avenue of investigation.^{6–9}

The SARS-CoV-2 genome contains two open reading frames (ORF1a and ORF1b). Translation of the genomic mRNA of ORF1a yields a polyprotein (pp1a), while a second polyprotein (pp1ab) is produced by a ribosomal frameshift that joins ORF1a together with ORF1b. The two polyproteins are processed by two cysteine proteases, a 3C-like protease (3CLpro) at 11

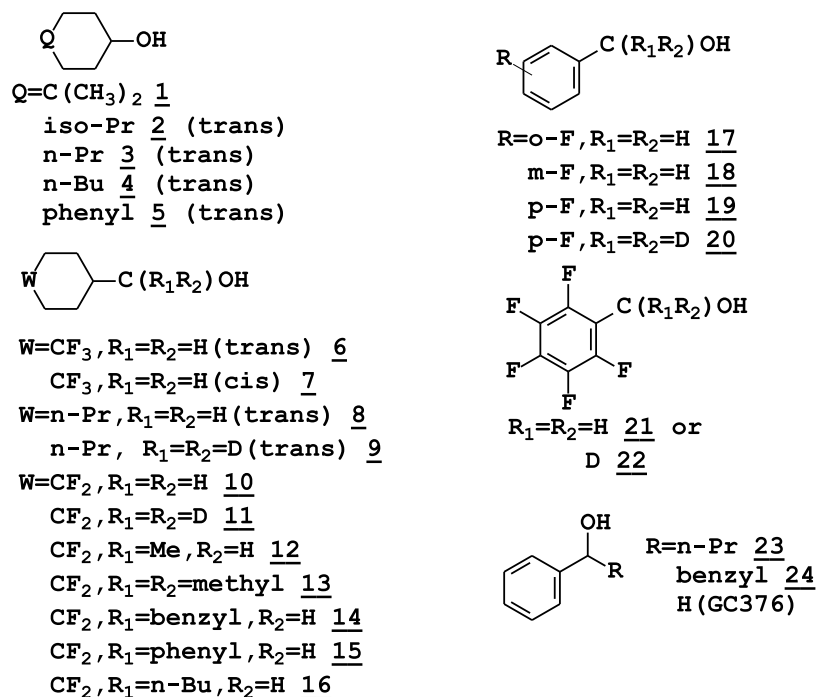
distinct cleavage sites and a papain-like protease (PLpro) at 3 distinct cleavage sites, resulting in 16 mature nonstructural proteins. The two proteases are essential for viral replication, making SARS-CoV-2 3CLpro an attractive target for therapeutic intervention.^{9–16}

SARS-CoV-2 3CLpro is a homodimer with a catalytic Cys–His dyad (Cys¹⁴⁵–His⁴¹) and an extended binding cleft. The protease displays a strong preference for a –Y–Z–Leu–Gln–X sequence, corresponding to the residues –P₄–P₃–P₂–P₁–P₁'-,¹⁷ where X is a small amino acid (Ser, Ala, Gly), Y is a small hydrophobic amino acid, and Z is solvent-exposed and can tolerate polar or nonpolar amino acid chains.¹⁸

Our foray in this area has focused on the structure-guided design of inhibitors of SARS-CoV-2 and MERS-CoV 3CLpro,^{19–21} as well as feline infectious peritonitis virus (FIPV) protease inhibitors.^{22,23} We recently described the structure-guided design of a dipeptidyl series of MERS-CoV and SARS-CoV-2 3CLpro inhibitors incorporating in their structure a piperidine²⁰ or cyclohexyl¹⁹ moiety capable of engaging in

Received: June 9, 2021

Table 1. Alcohol Inputs



Scheme 1

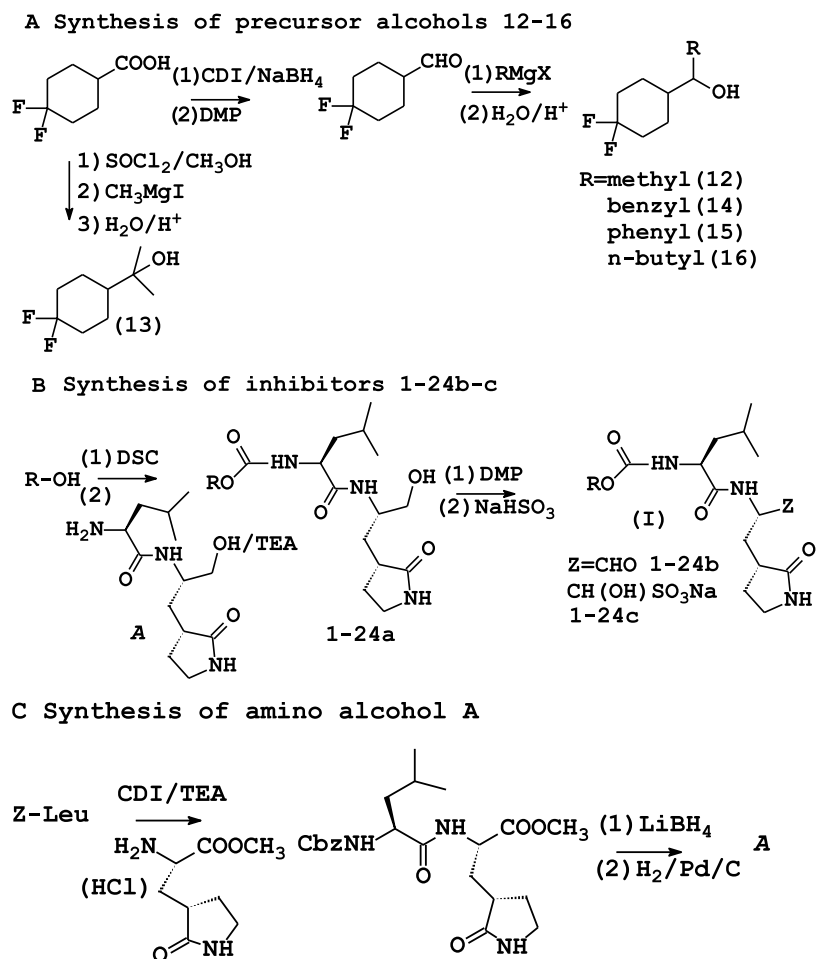


Table 2. IC₅₀ Values of Compounds 1–24b/c against SARS-CoV-2 3CLpro, IC₅₀ Values of Selected Compounds against MERS-CoV 3CLpro, EC₅₀ Values against SARS-CoV-2 3CLpro, and CC₅₀ Values of Selected Compounds

Compound Code	Structure	Z	IC ₅₀ (μM)		EC ₅₀ (μM) SARS-CoV-2	CC ₅₀ (μM)
			SARS-CoV-2	MERS-CoV		
1b		-CHO	0.25±0.05	0.12±0.02	3.48±0.05	> 100
1c		-CH(OH)SO ₃ Na	0.24±0.01	0.12±0.04	1.67±0.45	> 100
2b		-CHO	0.24±0.01	Not Determined		
2c		-CH(OH)SO ₃ Na	0.24±0.02			
3b		-CHO	0.25±0.02			
3c		-CH(OH)SO ₃ Na	0.19±0.02			
4b		-CHO	0.17±0.01	0.12±0.01	4.84±0.64	55±5
4c^b		-CH(OH)SO ₃ Na	0.18±0.01	0.15±0.01	4.23±1.54	58±8
5b		-CHO	0.22±0.03	Not Determined		
5c		-CH(OH)SO ₃ Na	0.23±0.04			
6b		-CHO	0.25±0.07			
6c		-CH(OH)SO ₃ Na	0.19±0.03			
7b		-CHO	0.23±0.04			
7c		-CH(OH)SO ₃ Na	0.20±0.03			
8b		-CHO	0.20±0.03	0.06±0.01	1.03±0.49	43±9
8c		-CH(OH)SO ₃ Na	0.20±0.01	0.11±0.01	4.43±0.35	44±4

Table 2. continued

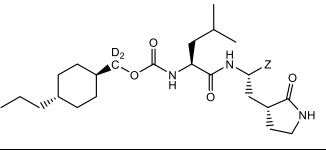
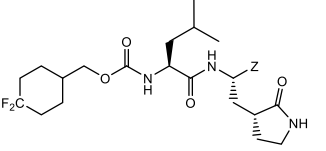
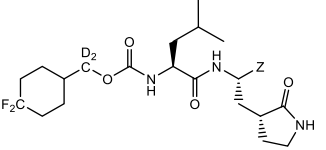
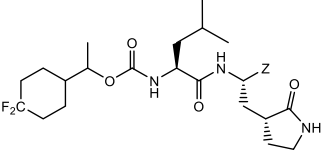
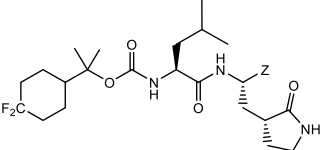
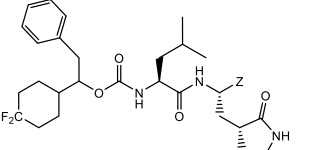
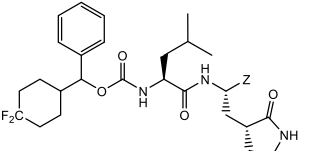
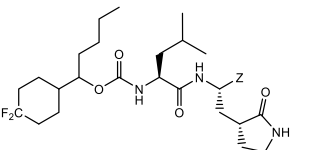
Compound Code	Structure	Z	IC ₅₀ (μM)		EC ₅₀ (μM)	CC ₅₀ (μM)
			SARS-CoV-2	MERS-CoV	SARS-CoV-2	
9b		-CHO	0.33±0.11	Not Determined		
9c		-CH(OH)SO ₃ Na	0.33±0.01			
10b^a		-CHO	0.48±0.08	0.08±0.01	Not Determined	
10c^a		-CH(OH)SO ₃ Na	0.45±0.10	0.10±0.01		
11b		-CHO	0.24±0.06	Not Determined		
11c		-CH(OH)SO ₃ Na	0.21±0.13			
12b		-CHO	0.26±0.07	Not Determined		
12c		-CH(OH)SO ₃ Na	0.26±0.08			
13b		-CHO	1.20±0.57	Not Determined		
13c		-CH(OH)SO ₃ Na	1.25±0.49			
14b		-CHO	0.31±0.11	0.10±0.02	2.95±0.94	> 100
14c		-CH(OH)SO ₃ Na	0.29±0.09	0.14±0.03	3.50±1.20	> 100
15b		-CHO	0.13±0.04	0.04±0.01	1.03±0.47	> 100
15c^b		-CH(OH)SO ₃ Na	0.17±0.01	0.05±0.01	1.45±0.42	> 100
16b		-CHO	0.19±0.04	Not Determined		
16c		-CH(OH)SO ₃ Na	0.27±0.03			

Table 2. continued

Compound Code	Structure	Z	IC ₅₀ (μM)		EC ₅₀ (μM)	CC ₅₀ (μM)
			SARS-CoV-2	MERS-CoV		
17b		-CHO	0.34±0.06	Not Determined		
17c		-CH(OH)SO ₃ Na	0.38±0.04			
18b		-CHO	0.35±0.04	0.07±0.01	5.28±2.62	> 100
18c		-CH(OH)SO ₃ Na	0.36±0.06	0.07±0.01	3.40±0.59	> 100
19b		-CHO	0.39±0.04	Not Determined		
19c		-CH(OH)SO ₃ Na	0.40±0.03			
20b		-CHO	0.39±0.06			
20c		-CH(OH)SO ₃ Na	0.32±0.06			
21b		-CHO	0.33±0.01	0.05±0.01	3.27±1.03	> 100
21c		-CH(OH)SO ₃ Na	0.36±0.01	0.08±0.01	4.84±0.64	> 100
22b		-CHO	0.47±0.23	Not Determined		
22c		-CH(OH)SO ₃ Na	0.60±0.21			
23b		-CHO	0.33±0.25	0.08±0.01	2.39±1.51	> 100
23c		-CH(OH)SO ₃ Na	0.21±0.04	0.13±0.01	3.72±1.60	> 100
24b		-CHO	0.50±0.16	Not Determined		
24c		-CH(OH)SO ₃ Na	0.31±0.01			

^aIC₅₀'s taken from Rathnayake et al.¹⁹ ^bEC₅₀: 0.85 ± 0.1 and 0.70 ± 0.08 μM for 4c and 15c, respectively, from live SARS-CoV-2 in Vero E6 cells.

favorable binding interactions with the S₄ pocket. We furthermore demonstrated that members of the cyclohexyl series of compounds improve survival in a mouse model of MERS-CoV infection.¹⁹ In this report, we established a cell-based assay to screen inhibitors against SARS-CoV-2 3CLpro, which is safe (BSL2) and fast (takes less than 24 h). Furthermore, we report the results of structure-guided studies

intended to interrogate the effects of stereochemistry, conformation, and structure, including the systematic introduction of fluorine (F-walk)^{24,25} around the structure of GC376^{21–23} and the synthesis of deuterated inhibitors,^{26–28} to modulate pharmacological activity, pharmacokinetic (PK) properties, and oral bioavailability.

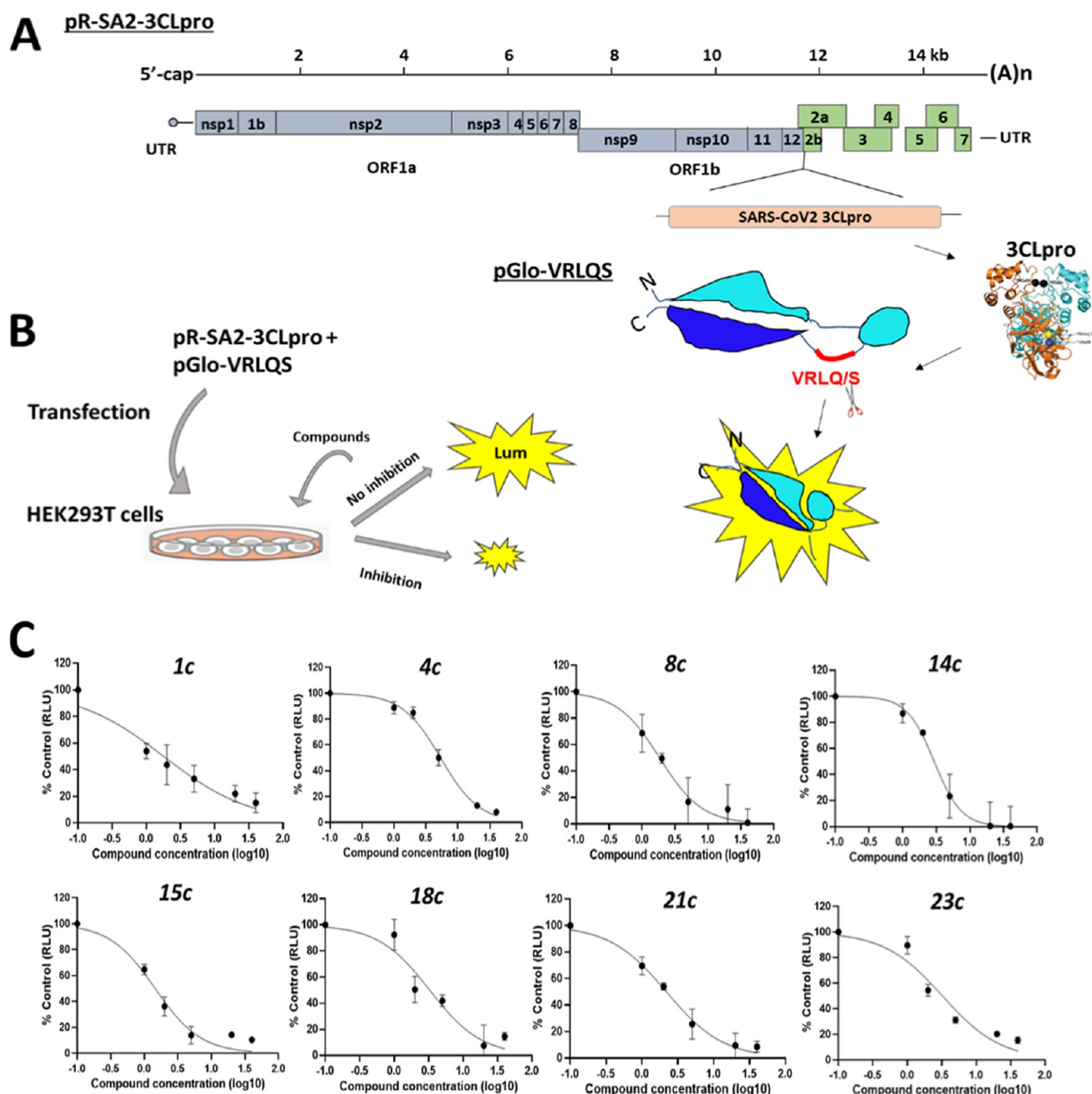


Figure 1. Generation of a cell-based assay for screening SARS-CoV-2 3CLpro inhibitors in HEK293T cells. Panel (A) Plasmid 1; pR-SA2-3CLpro encodes SARS-CoV-2 3CLpro from the PRRSV reverse genetics system. The gene of SARS-CoV-2 3CLpro is inserted between ORF1b and 2a of PRRSV genome. Plasmid 2; pGlo-VRLQS encodes firefly luciferase with coronavirus 3CLpro recognition sequences VRLQS. Active luciferase is generated by the cleavage with CoV 3CLpro. Panel (B) Semiconfluent HEK293T cells were transfected with two plasmids, and after overnight, various concentrations of each compound are applied to the cells. The inhibition of SARS-CoV-2 3CLpro is determined by measuring luciferase activity. Panel (C) Inhibition curves of selected compounds, 1c, 4c, 8c, 14c, 15c, 18c, 21c, and 23c, using the cell-based assay with pR-SA2-3CLpro and pGlo-VRLQS.

RESULTS AND DISCUSSION

Chemistry. The synthesis of compounds 1–24b/c entailed the use of a structurally diverse set of precursor alcohols (Table 1), some of which were commercially available. Alcohols 12–16 were readily synthesized from 4,4-difluorocyclohexane carboxylic acid via reduction to the corresponding alcohol by treatment with carbonyl diimidazole and sodium borohydride,²⁹ followed by oxidation with Dess–Martin periodinane reagent to yield the aldehyde. Subsequent treatment with an array of Grignard

reagents generated alcohols 12 and 14–16 (Scheme 1/panel A). Alcohol 13 was synthesized by reacting the methyl ester of 4,4-difluorocyclohexane carboxylic acid with excess methyl magnesium iodide, followed by acidic workup (Scheme 1/panel A). Deuterated alcohols 9, 11, 20, and 22 were obtained by treatment of the precursor carboxylic acid with carbonyl diimidazole followed by the addition of sodium borodeuteride. All trans-substituted alcohols were synthesized by reducing the

precursor 4-substituted cyclohexanone with sodium borohydride/CeCl₃.³⁰

Compounds 1–24b/c were readily obtained by reacting each precursor alcohol with disuccinimidyl carbonate,³¹ followed by coupling with amino alcohol A. The resulting product was treated with Dess–Martin periodinane to yield aldehydes 1–24b, which were converted to the corresponding bisulfite adducts 1–24c upon treatment with sodium bisulfite (Scheme 1/panel B).³² An alternative synthesis was used in the case of compounds 6–8, 10–16, 23, and 24, which involved the reaction of the precursor alcohol with (L) leucine methyl ester isocyanate, as described in detail previously.³³ The synthesis of precursor amino alcohol A was readily accomplished by coupling (L) Z-Leu with a glutamine surrogate, followed by sequential reduction with LiBH₄ and removal of the protective group (H₂/Pd) (Scheme 1/panel C).

Biochemical Studies. Enzyme Assays. The inhibitory activity of compounds 1–24b/c against SARS-CoV-2 3CLpro in biochemical assays was determined as described in the Experimental Section. The IC₅₀ values against SARS-CoV-2 and MERS-CoV-2 in the enzyme assays are summarized in Table 2, and they are the average of at least two determinations. Most of the compounds potently inhibited SARS-CoV-2 3CLpro and displayed IC₅₀ values that ranged between 0.13 and 1.25 μM. Compounds 15b and 15c were the most effective against SARS-CoV-2 3CLpro, with IC₅₀ values 0.13 and 0.17 μM, respectively. The inhibitory activity of a select number of compounds against MERS-CoV 3CLpro was also investigated. The compounds were found to be 3–5-fold more potent against MERS-CoV-3CLpro, with IC₅₀ values in the 40–150 nM range (Table 2). Interestingly, compounds 15b and 15c were the most effective against MERS-CoV-3CLpro as well, with IC₅₀ values 0.04 and 0.05 μM, respectively. The broad spectrum of inhibitory activity displayed by these compounds enhances their therapeutic potential.

Establishment of the Cell-Based Assay for SARS-CoV-2 3CLpro Inhibitors. We have previously reported EC₅₀ values determined by incubating SARS-CoV-2 3CLpro inhibitors and Vero E6 cells that were inoculated with SARS-CoV-2 at 50–100 plaque forming units/well.^{19,33} This cell-based assay requires a BSL3 facility and takes at least 2–3 days. As an alternative method, we report herein a relatively fast and safe cell-based assay system to screen SARS-CoV-2 3CLpro inhibitors using two plasmids. A similar cell-based assay has been reported;³⁴ however, in contrast, the present system utilizes the replication units of porcine respiratory and reproductive syndrome virus (PRRSV)³⁵ to express SARS-CoV-2 3CLpro. In this system, plasmid 1, pR-SARS-CoV-2 3CLpro, was used to express SARS-CoV-2 3CLpro, whereas plasmid 2, pGlo-VRLQS, was used to express luciferase-VRLQS in HEK293T cells (Figure 1/panel A). The expressed inactive luciferase is activated by the catalytic mechanism of SARS-CoV-2 3CLpro in HEK293T cells. Hence, the inhibition of SARS-CoV-2 3CLpro was measured as a function of firefly luciferase activity (Figure 1/panel B). Plasmid 2 also contains intact Renilla luciferase gene as an expression control. As a negative control, the inactive form of the 3CLpro was introduced to pR-SARS-CoV-2 3CLpro by the mutagenesis, and the resulting plasmid was designated as pR-SARS-CoV-2 3CLpro C145A. The mock-transfection was also used as a negative control. The expression of coronavirus 3CLpro was reported to induce cytotoxicity in the transfected cells.^{36,37} The level of cytotoxicity in our assay system was about 7%, and the ratio of firefly to Renilla luminescence was adjusted to reduce

variability due to cytotoxicity and transfection efficiency. The EC₅₀ values of a select number of compounds, including 1b/1c, 4b/4c, 8b/8c, 14b/14c, 15b/15c, 18b/18c, 21b/21c, and 23b/23c, were determined (Table 2). Inhibition curves by each compound were consistent with a dose-dependent mode and R² > 0.8 (Figure 1/panel C). The IC₅₀ and EC₅₀ values of 15b and 15c were the lowest among tested compounds listed in Table 2.

For comparative purposes, we determined EC₅₀ values using live SARS-CoV-2 in Vero E6 cells and the established two-plasmid system of two compounds (4c, 15c) from this work and a previously published 3CLpro inhibitor, GC376. Compounds 4c and 15c were selected on the basis of having the lowest IC₅₀ values in this series. The EC₅₀ of GC376 was found to be 0.23 ± 0.01 μM in live SARS-CoV-2 in Vero E6 cells.³³ In the two-plasmid system, the EC₅₀ of GC376 was determined to be 3.15 ± 0.67 μM (14-fold higher), and the R² values of the inhibition curves were >0.9. When the antiviral effects of compounds 4c and 15c were examined from live SARS-CoV-2 in Vero E6 cells, the EC₅₀ values were 0.85 ± 0.1 and 0.70 ± 0.08 μM, respectively (Table 2). The results show that while compounds in this series are cell-permeable, the EC₅₀ values were higher from the two-plasmid system (2-fold for 15c and 5-fold for 4c) than those by live SARS-CoV-2 in Vero E6 cells. The higher EC₅₀s may be due to various reasons including different cell types, presence of transfection reagent, incubation time, and overexpression of the 3CLpro and luciferase in HEK293T cells due to inhibition of cytotoxic 3CLpro in the two-plasmid system.^{36,37} Most of the examined compounds showed minimal toxicity up to 100 μM; however, the CC₅₀ values for 4b/4c and 8b/8c were in the 40–60 μM range (Table 2). Although the EC₅₀ values obtained from the two-plasmid system are higher than those obtained from live SARS-CoV-2 in Vero E6 cells, considering the feasibility of conducting the experiments under BSL2 laboratory conditions and the relatively short amount of time required (24 h), the cell-based two-plasmid method could be a useful initial screening tool for 3CLpro inhibitors against SARS-CoV-2.

X-ray Crystallographic Studies. A series of high-resolution cocrystal structures were determined to elucidate the interaction of the inhibitors with the active site of SARS-CoV-2 3CLpro. Specifically, we sought to confirm the mechanism of action, identify the structural determinants associated with the binding of the inhibitors to the active site of the protease, and ultimately harness the accumulated structural information and insights gained to further optimize pharmacological activity and PK parameters. Three groups of inhibitor types were analyzed with respect to their structural elements that interact within the S₄ subsite environment, which are (1) nonpolar substituents (Table 2, entries 1–9), (2) 4,4-difluorocyclohexyl groups that are connected to a stereocenter (Table 2, entries 10–16), and (3) fluorinated aryl compounds based on the structure of GC376 (Table 2, entries 17–22).

For all structures described below, the active sites contained prominent difference electron density consistent with inhibitors covalently bound to Cys 145. Additionally, the electron density was consistent with both the R and S enantiomers at the stereocenter formed by covalent attachment of the S_γ atom of Cys 145 and were therefore modeled as each enantiomer with 0.5 occupancy. The γ-lactam ring of the inhibitor forms direct hydrogen bonds with Glu 166 and His163, and Glu 166 and Gln 189 form additional H-bonds with the C=O and NH of the carbamate moiety in the inhibitor. The inhibitor engages in hydrophobic interactions with the leucine side chain, which is

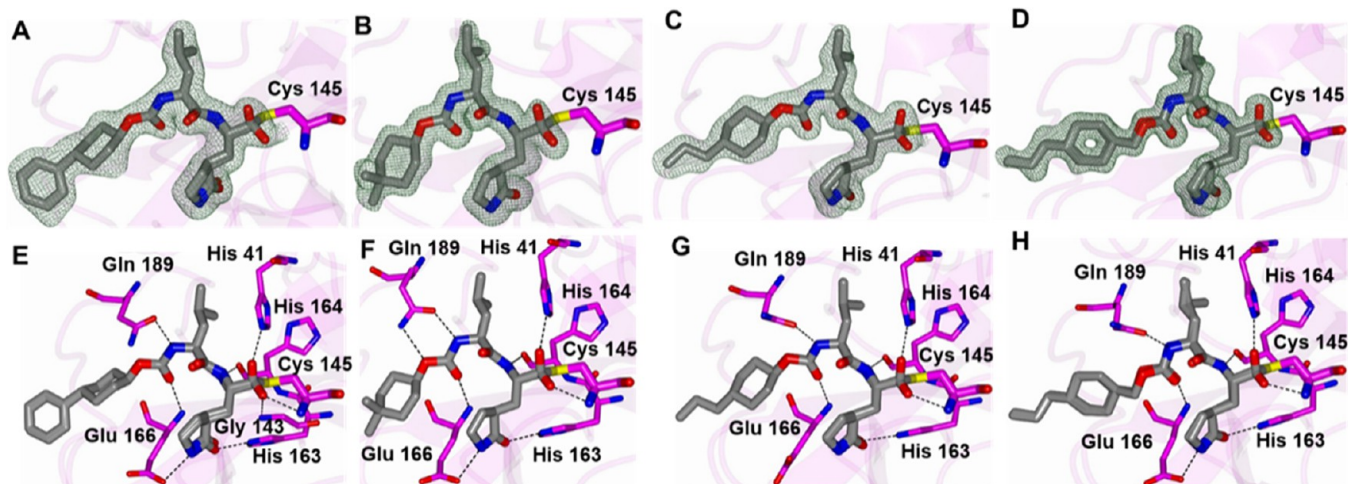


Figure 2. Binding mode of inhibitors containing nonpolar substituents. **5c** (A/E), **1c** (B/F), **3c** (C/G), and **8b** (D/H) with SARS-CoV-2 3CLpro. Fo–Fc Polder omit map (A–D) contoured at 3σ . Hydrogen bond interactions (E–H) are drawn as dashed lines. PDB IDs: **5c** (7LZZ), **1c** (7LZX), **3c** (7LZY), and **8b** (7LZT).

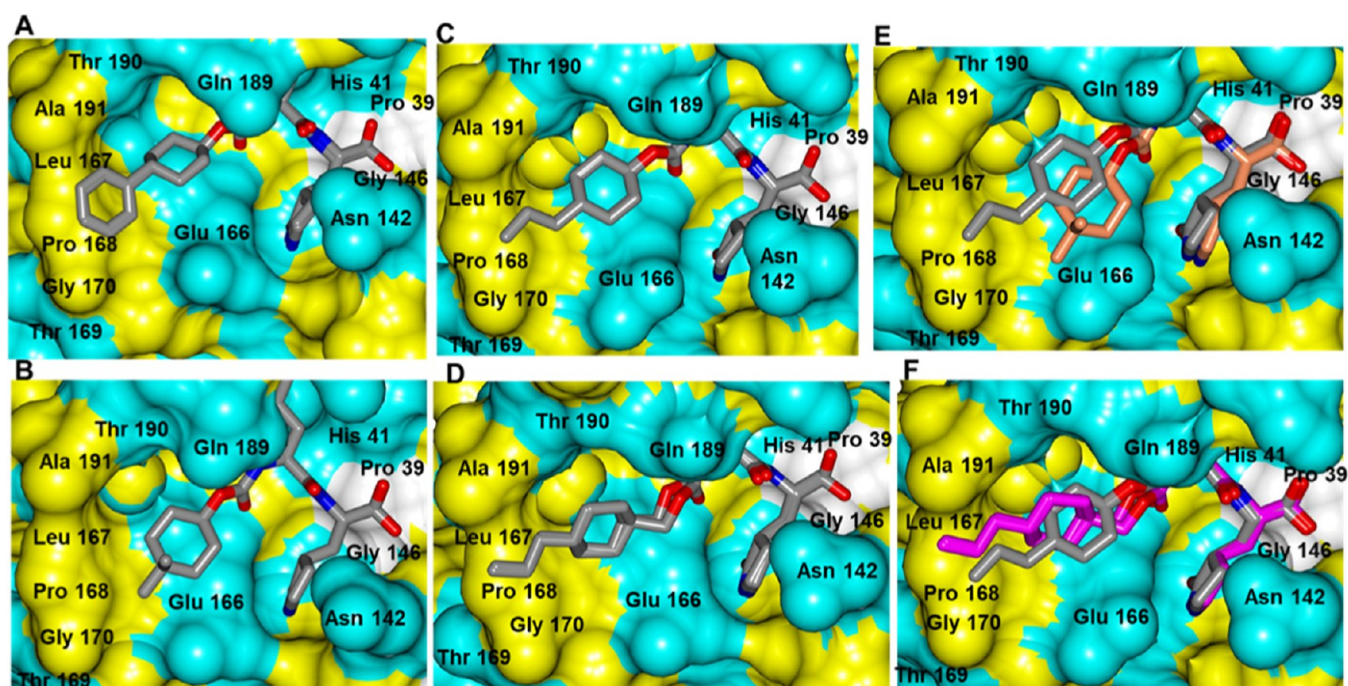


Figure 3. Surface representation showing the orientation of nonpolar groups near the S_4 subsite of SARS-CoV-2 3CLpro, with neighboring residues colored yellow (nonpolar), cyan (polar), and white (weakly polar). **5c** (A), **1c** (B), **3c** (C), and **8b** (D). Superposition of **3c** (gray) and **1c** (coral) (E). Superposition of **3c** (gray) and **8b** (magenta) (F). PDB IDs: **5c** (7LZZ), **1c** (7LZX), **3c** (7LZY), and **8b** (7LZT).

snugly accommodated in the S_2 pocket. The cocrystal structure confirms that the reaction of Cys145 with the aldehyde warhead results in the formation of a tetrahedral hemithioacetal that is stabilized by a H-bond to His164.

Nonpolar Substituents. The structures of **5c**, **1c**, **3c**, and **8b** displayed well-defined electron densities and similar hydrogen bond interactions, as shown in Figure 2. For all structures, the nonpolar groups are mainly positioned within the S_4 subsite near a hydrophobic ridge formed by residues Leu 167, Pro 168, Gly 170, and Ala 191 (Figure 3). However, the dimethylcyclohexyl ring in **1c** is too short to fully engage the hydrophobic ridge in the S_4 subsite (Figure 3B). The addition of an *n*-propyl group in **3c** permits further engagement with the hydrophobic cleft, and the extra carbon atom in **8b** allows the propyl group to extend

even further (Figure 3C,D). Superposition of **3c** and **1c** (Figure 3E) shows that the 4,4-dimethylcyclohexyl ring is moved slightly out of the S_4 subsite relative to the *n*-propyl group in **3c**. Additionally, the superposition of **3c** and **8b** revealed quite similar binding modes although the *n*-propyl group of **8b** is positioned deeper within the S_4 subsite (Figure 3F). Overall, the similar binding modes and attendant high potency of the inhibitors are reflected in their low IC_{50} values and similar potencies (Table 2, compounds **1–5b/c**). With respect to compound **8**, it was envisaged that the corresponding deuterated compound **9**, found to be nearly equipotent to nondeuterated compound **8** (Table 2), would likely display improved PK properties due to its enhanced *in vivo* stability arising from the

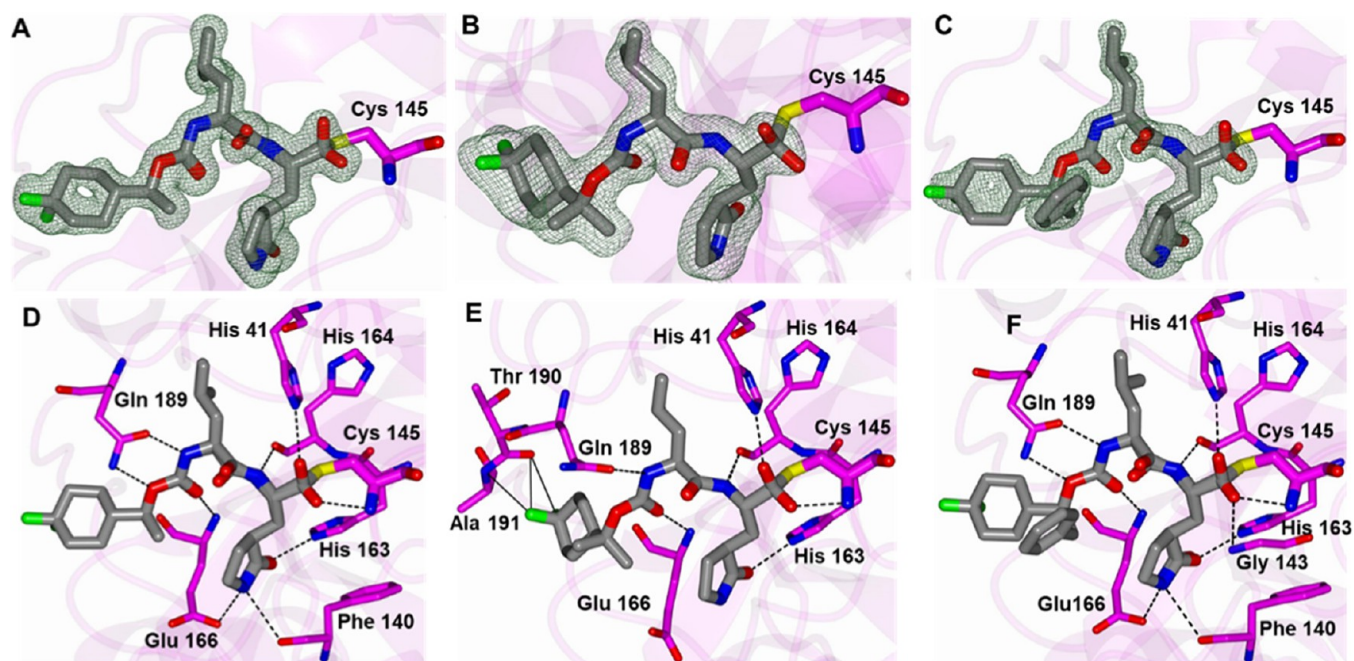


Figure 4. Binding mode of inhibitors containing a 4,4-difluorocyclohexyl group. **12b** (A/D), **13c** (B/E), and **14c** (C/F) with SARS-CoV-2 3CLpro. Fo–Fc Polder omit map (A–C) contoured at 3σ . Hydrogen bond interactions (D–F) are drawn as dashed lines. PDB IDs: **12b** (7LZU), **13c** (7M00), and **14c** (7M01).

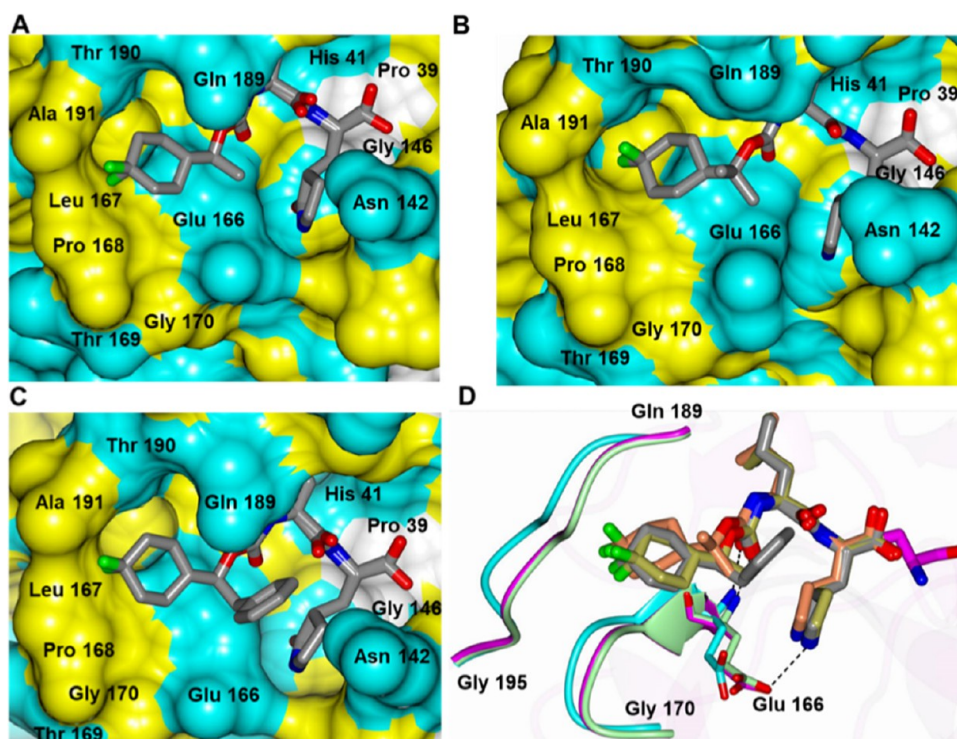


Figure 5. Surface representation showing the orientation of the 4,4-difluorocyclohexyl groups near the S4 subsite of SARS-CoV-2 3CLpro, with neighboring residues colored yellow (nonpolar), cyan (polar), and white (weakly polar). **12b** (A), **13c** (B), and **14c** (C). Superposition of **12b** (gold), **13c** (coral), and **14c** (gray) (D). The loop between Gln 189 and Gly 195 is colored cyan for **13c** and magenta for **12b/14c**. Hydrogen bond interactions with Glu 166 are indicated by the dashed lines. PDB IDs: **12b** (7LZU), **13c** (7M00), and **14c** (7M01).

greater strength of the C–D bond and the resulting deuterium kinetic isotope effect.^{26–28}

4,4-Difluorocyclohexyl Compounds. In previous studies related to norovirus 3CLpro inhibitors, the strategic introduction of a *gem*-dimethyl group into the inhibitor structure resulted

in enhanced potency by restricting the rotation around the nearby single bonds and lowering the entropic penalty associated with binding.³⁸ Thus, we sought to capitalize on this by synthesizing *gem*-dimethyl-substituted compound **13c** and, additionally, achieve the same end by introducing a

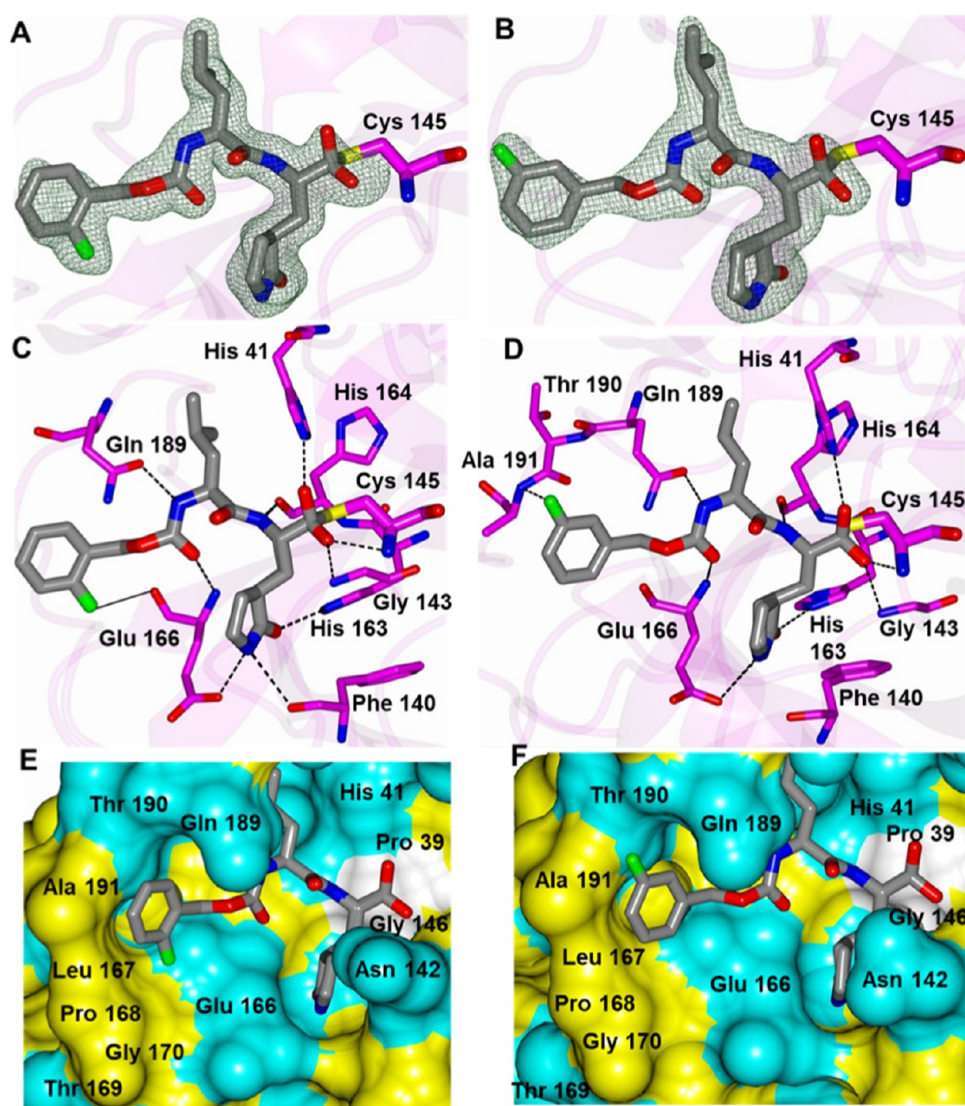


Figure 6. Binding mode of inhibitors containing a fluorinated aromatic group. 17c (A/C) and 18c (B/D) with SARS-CoV-2 3CLpro. Fo–Fc Polder omit map (A, B) contoured at 3σ . Hydrogen bond interactions (C, D) are drawn as dashed lines. The 3.38 Å contact between the F-atom of 17c and the backbone O-atom of Glu 166 is drawn as a solid line in panel (C). Surface representation of 17c (E) and 18c (F) showing the orientation of the 4,4-difluorocyclohexyl groups near the S_4 subsite of SARS-CoV-2 3CLpro, with neighboring residues colored yellow (nonpolar), cyan (polar), and white (weakly polar). PDB IDs: 17c (7M02) and 18c (7M03).

stereocenter (12c). The structures of 12b, 13c, and 14c with SARS-CoV 3CLpro displayed well-defined electron densities and the typically observed hydrogen bond interactions (Figure 4). The 4,4-difluorocyclohexyl rings for all structures are positioned near the hydrophobic cleft in the S_4 subsite, as shown in Figure 5A–C. Superposition of these structures revealed a nearly identical binding mode for 12b and 13c in which the 4,4-difluorocyclohexyl groups are positioned in the same region within the S_4 subsite (Figure 5D). For 14c, the benzyl ring is oriented in a wide cleft formed by Asn 142 and Gln 189. However, the 4,4-difluorocyclohexyl ring of 13c contacts residues Thr 190 and Ala 191 (3.0–3.2 Å) and forms new hydrogen bond interactions with the backbone oxygen and nitrogen atoms, respectively (Figure 4E). This positions the 4,4-difluorocyclohexyl ring of 13c deeper into the S_4 pocket and results in a conformational change in the loop spanning Gln 189 to Gly 195 and Glu 166 to Gly 170 to accommodate the new interactions and avoid steric clash. This results in the loss of the typical hydrogen bond between the side chain of Glu 166 and

the glutamine surrogate of 13c (Figures 4E and 5D), which may explain why the IC_{50} of 13c is ~ 4 -fold higher than those of 12b and 14c.

Fluorinated Aryl Compounds. Positional analogue scanning is a widely used strategy for optimizing binding affinity, selectivity, and physicochemical properties of lead compounds containing aromatic or heteroaromatic rings.²⁴ For instance, the introduction of fluorine (F-walk)²⁵ or nitrogen (N-walk)³⁹ is an effective means for multiparameter optimization by leveraging the beneficial impact of fluorine (or nitrogen) and minor structural changes. In an effort to determine the effect of fluorine on the binding mode in the S_4 subsite of GC376, the structures of the fluorinated benzyl compounds 17c, 18c, 19b, 20b (deuterated analogue of 19b), and 21c were determined with SARS-CoV-2 3CLpro. The inhibitor *o*-fluorobenzyl (17c) and *m*-fluorobenzyl (18c) compounds displayed well-defined electron densities and similar hydrogen bond interactions, as shown in Figure 6. Interestingly, the *o*-fluorobenzyl ring of 17c adopts a conformation in which the fluorine atom is directed

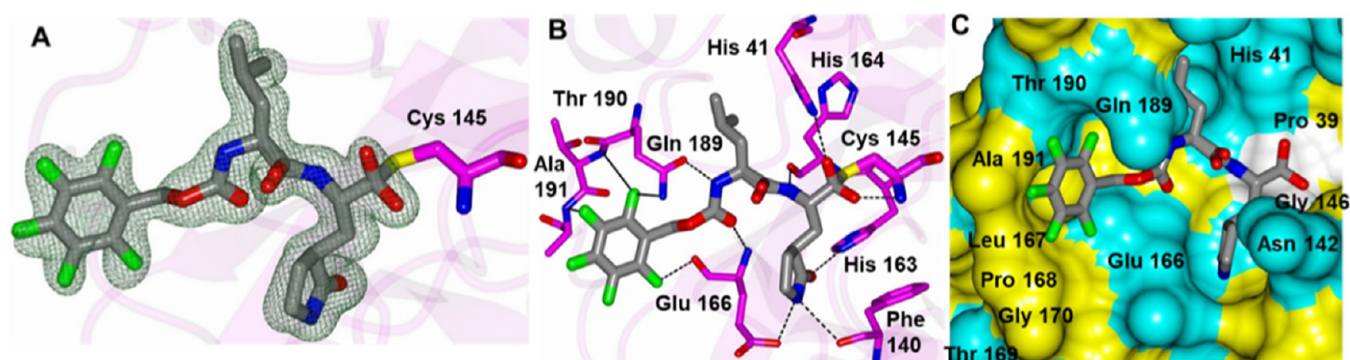


Figure 7. Binding mode of **21c** containing a perfluorinated aromatic group. Fo–Fc Polder omit map contoured at 3σ (A). Hydrogen bond interactions are drawn as dashed lines. Close contacts to the perfluorinated ring that are longer than typical polar contact distances are drawn as solid lines (B). Surface representation showing the orientation of **21c** near the S₄ subsite of SARS-CoV-2 3CLpro, with neighboring residues colored yellow (nonpolar), cyan (polar), and white (weakly polar) (C). PDB ID: **21c** (7M04).

away from Thr 190 and is instead positioned 3.38 Å from the backbone oxygen atom of Glu 166 (Figure 6C). Conversely, the fluorine atom in **18c** is positioned between Thr 190/Ala 191 in the S₄ pocket and is 3.10 Å from the backbone nitrogen atom of Ala 191 (Figure 6D). The orientations of the fluorine atoms in **17c** and **18c** relative to the hydrophobic ridge in the S₄ pocket are shown in Figure 6E,F.

The compounds that contain a *p*-fluorobenzyl group **19b** and its deuterated analogue **20b** not surprisingly adopt very similar binding modes and hydrogen bond interactions, as shown in Figures S1 and S2. Interestingly, the inhibitor adopts two conformations in which the *p*-fluorobenzyl ring is projected away from the S₄ subsite in subunit B and is positioned in the S₄ pocket in subunit A. However, the electron density for the *p*-fluorobenzyl ring is somewhat weaker in subunit A, which suggests that the pose in subunit B is likely the predominant conformation. This may be due to the fact that the fluorine atom does not form any contacts with polar atoms in the S₄ subsite and results in a conformation in which the aryl ring is positioned out of the pocket, which is the same conformation observed for the parent compound GC376.

The perfluorinated compound **21c** also displayed a well-defined difference electron density consistent with the aryl ring in one conformation (Figure 7A). Interestingly, one of the *o*-fluorine atoms interacts with the backbone oxygen of Glu 166 (3.08 Å), which is shorter than that observed for **17c** described above (3.38 Å). The other *o*-fluorine atom is positioned 2.92 Å from the backbone N-atom of Thr 190 and 3.12 Å from the side chain N-atom of Gln 189 (Figure 7B). Similarly, the *m*-fluorine atom is positioned near the backbone nitrogen atom of Ala 191 (3.40 Å), which is longer than the distance observed for **18c** (3.10 Å). The pentafluorobenzyl ring is positioned on top of the hydrophobic cleft within the S₄-subsite (Figure 7C), unlike GC376 where the phenyl ring undergoes a hydrophobic collapse with the γ -lactam ring and the inhibitor assumes a “paper clip” shape.

Finally, GC376 variants **23b/c** and **24b/c** were synthesized and screened as mixtures of epimers. The aldehyde and bisulfite adduct compounds **23b/c** were found to potently inhibit 3CLpro (IC₅₀ 0.15 and 0.18 μ M, respectively), and these were 27- and 19-fold more potent than the corresponding **24b/c** aldehyde and bisulfite adducts, respectively. These findings provide tentative validation of the design regarding the use of a chiral center to attain directional control and augment binding interactions.

CONCLUSIONS

Effective management of SARS-CoV-2, the causative agent of the COVID-19 pandemic, would require the availability of safe and effective vaccines (already realized), as well as the availability of small-molecule therapeutics and prophylactics that target viral- and host-based druggable targets. SARS-CoV-2 3CLpro is an attractive target for the development of COVID-19 therapeutics because of its vital role in viral replication. An array of approaches was utilized to optimize potency and physicochemical parameters, including conformational and stereochemical control via the introduction of a *gem*-dimethyl group (Thorpe–Ingold effect) or stereocenter, deuteration, and fluorine, into the inhibitors. Virtually, all inhibitors were found to display a submicromolar potency against SARS-CoV-2 and MERS-CoV 3CLpro, and the inhibitory activities were confirmed by a newly established fast and safe cell-based assay. Furthermore, several deuterated inhibitors, which are likely to exhibit improved pharmacokinetics, were found to be equipotent with the corresponding nondeuterated inhibitors. The fluorine-walk approach was applied to explore bioisosteric replacements for the phenyl ring in GC376 by replacing one or more hydrogen atoms. The effects of these modifications included unanticipated binding modes of the F-substituted phenyl ring and modestly enhanced potency. The introduction of multiple fluorine atoms resulted in an orientation that allowed the fluorine atoms to engage in H-bonding with residues in the S₄ pocket, although with suboptimal bond angles. High-resolution cocrystal structures with an array of inhibitors unraveled the mechanism of action and provided valuable insights regarding the binding of the inhibitors to the active site and the identity of the structural determinants involved in binding. The 4,4-difluorocyclohexane methyl moiety connected to the benzylic carbon, coupled with the directional control imparted by the chiral center, resulted in a near-optimal fit in this series (Table 2, entry 15). Collectively, the results of the studies described herein are significant and timely and provide an effective launching pad for conducting further preclinical studies.

EXPERIMENTAL SECTION

General. Reagents and dry solvents were purchased from various chemical suppliers (Sigma-Aldrich, Acros Organics, Chem-Impex, TCI America, Oakwood Chemical, APExBIO, Cambridge Isotopes, Alpha Aesar, Fisher, and Advanced Chemblocks) and were used as obtained. Silica gel (230–450 mesh) used for flash chromatography was

purchased from Sorbent Technologies (Atlanta, GA). Thin-layer chromatography was performed using Analtech silica gel plates. Visualization was accomplished using UV light and/or iodine. NMR spectra were recorded in CDCl₃ or DMSO-*d*₆ using a Varian XL-400 spectrometer. The purity of most of the aldehyde inhibitors was found to be ≥95%, determined by absolute qNMR analysis using a Bruker AV III 500 equipped with a CPDUL CRYOprobe and CASE autosampler at the KU NMR lab.⁵⁴ Dimethyl sulfone TraceCERT was used as the internal calibrant. High-resolution mass spectrometry (HRMS) was performed at the Wichita State University Mass Spectrometry lab using an Orbitrap Velos Pro mass spectrometer (ThermoFisher, Waltham, MA) equipped with an electrospray ion source.

Synthesis of Compounds. Preparation of Compounds 1–5a, 9a, and 17–22a. General Procedure. To a solution of alcohol (1 equiv) (Table 1) in anhydrous acetonitrile (10 mL/g alcohol) were added *N,N'*-disuccinimidyl carbonate (1.2 equiv) and triethyl amine (TEA) (3.0 equiv), and the reaction mixture was stirred for 4 h at room temperature. The solvent was removed *in vacuo*, and the residue was dissolved in ethyl acetate (40 mL/g alcohol). The organic phase was washed with saturated aqueous NaHCO₃ (2 × 20 mL/g alcohol), followed by brine (20 mL/g alcohol). The organic layers were combined and dried over anhydrous Na₂SO₄, filtered, and concentrated *in vacuo* to yield the mixed carbonate, which was used in the next step without further purification.

To a solution of Leu–Gln surrogate amino alcohol (1.0 equiv) in dry methylene chloride (10 mL/g of amino alcohol) was added TEA (1.5 equiv), and the reaction mixture was stirred for 20 min at room temperature (solution 1). In a separate flask, the mixed carbonate was dissolved in dry methylene chloride (10 mL/g of carbonate) (solution 2). Solution 1 was added to solution 2, and the reaction mixture was stirred for 3 h at room temperature. Methylene chloride was added to the organic phase (40 mL/g of carbonate) and then washed with saturated aqueous NaHCO₃ (2 × 20 mL/g alcohol), followed by brine (20 mL/g alcohol). The organic phase was dried over anhydrous Na₂SO₄, filtered, and concentrated *in vacuo*. The resultant crude product was purified by flash chromatography (hexane/ethyl acetate) to yield dipeptidyl alcohol as a white solid.

4,4-Dimethylcyclohexyl-((S)-1-(((S)-1-hydroxy-3-((S)-2-oxopyrrolidin-3-yl)propan-2-yl)amino)-4-methyl-1-oxopentan-2-yl)-carbamate (1a). Yield (36%), ¹H NMR (400 MHz, DMSO-*d*₆) δ 7.57 (d, *J* = 8.9 Hz, 1H), 7.51 (s, 1H), 7.07 (d, *J* = 8.3 Hz, 1H), 4.67–4.63 (m, 1H), 4.47–4.40 (m, 1H), 3.98–3.88 (m, 1H), 3.78–3.74 (m, 1H), 3.36–3.28 (m, 1H), 3.27–3.17 (m, 1H), 3.13 (t, *J* = 8.9 Hz, 1H), 3.09–2.98 (m, 1H), 2.26–2.16 (m, 1H), 2.15–2.10 (m, 1H), 1.83–1.72 (m, 1H), 1.68–1.63 (m, 2H), 1.62–1.50 (m, 2H), 1.48–1.30 (m, 6H), 1.25–1.13 (m, 3H), 0.92–0.81 (m, 12H).

(1*r*,4*S*)-4-Iso-propylcyclohexyl-((S)-1-(((S)-1-hydroxy-3-((S)-2-oxopyrrolidin-3-yl)propan-2-yl)amino)-4-methyl-1-oxopentan-2-yl)-carbamate (2a). Yield (35%), ¹H NMR (400 MHz, DMSO-*d*₆) δ 7.57 (d, *J* = 8.9 Hz, 1H), 7.51 (s, 1H), 7.07 (d, *J* = 8.2 Hz, 1H), 4.65 (t, *J* = 5.5 Hz, 1H), 4.34 (td, *J* = 11.0, 5.5 Hz, 1H), 3.97–3.88 (m, 1H), 3.79–3.74 (m, 1H), 3.38–3.28 (m, 1H), 3.27–3.18 (m, 1H), 3.14 (t, *J* = 9.0 Hz, 1H), 3.05 (q, *J* = 8.5 Hz, 1H), 2.29–2.20 (m, 1H), 2.18–2.07 (m, 1H), 1.91 (d, *J* = 7.9 Hz, 2H), 1.84–1.72 (m, 1H), 1.71–1.66 (m, 2H), 1.62–1.50 (m, 2H), 1.48–1.30 (m, 4H), 1.26–1.13 (m, 2H), 1.01 (s, 3H), 0.93–0.80 (m, 12H).

(1*s*,4*S*)-4-Propylcyclohexyl-((S)-1-(((S)-1-hydroxy-3-((S)-2-oxopyrrolidin-3-yl)propan-2-yl)amino)-4-methyl-1-oxopentan-2-yl)-carbamate (3a). Yield (38%), ¹H NMR (400 MHz, DMSO-*d*₆) δ 7.57 (d, *J* = 9.0 Hz, 1H), 7.51 (s, 1H), 7.07 (d, *J* = 8.2 Hz, 1H), 4.65 (s, 1H), 4.36 (td, *J* = 11.0, 5.5 Hz, 1H), 3.98–3.88 (m, 1H), 3.78–3.74 (m, 1H), 3.36–3.29 (m, 1H), 3.28–3.18 (m, 1H), 3.14 (t, *J* = 8.9 Hz, 1H), 3.10–2.99 (m, 1H), 2.30–2.19 (m, 1H), 2.17–2.07 (m, 1H), 1.93–1.84 (m, 2H), 1.77–1.67 (m, 3H), 1.62–1.48 (m, 2H), 1.48–1.30 (m, 3H), 1.33–1.21 (m, 3H), 1.21–1.08 (m, 4H), 0.97–0.90 (m, 2H), 0.90–0.81 (m, 9H).

(1*s*,4*S*)-4-Butylcyclohexyl-((S)-1-(((S)-1-hydroxy-3-((S)-2-oxopyrrolidin-3-yl)propan-2-yl)amino)-4-methyl-1-oxopentan-2-yl)-carbamate (4a). Yield (35%), ¹H NMR (400 MHz, DMSO-*d*₆) δ 7.57 (d, *J* = 9.0 Hz, 1H), 7.51 (s, 1H), 7.07 (d, *J* = 8.2 Hz, 1H), 4.65 (t, *J* = 5.5 Hz, 1H), 4.36 (tt, *J* = 10.9, 4.2 Hz, 1H), 3.98–3.88 (m, 1H), 3.79–3.74

(m, 1H), 3.38–3.28 (m, 1H), 3.28–3.18 (m, 1H), 3.14 (t, *J* = 8.9 Hz, 1H), 3.10–2.99 (m, 1H), 2.30–2.18 (m, 1H), 2.18–2.07 (m, 1H), 1.93–1.84 (m, 2H), 1.79–1.65 (m, 3H), 1.62–1.50 (m, 2H), 1.48–1.30 (m, 3H), 1.29–1.14 (m, 9H), 0.97–0.90 (m, 2H), 0.90–0.81 (m, 9H).

(1*r*,4*S*)-4-Phenylcyclohexyl-((S)-1-(((S)-1-hydroxy-3-((S)-2-oxopyrrolidin-3-yl)propan-2-yl)amino)-4-methyl-1-oxopentan-2-yl)-carbamate (5a). Yield (51%), ¹H NMR (400 MHz, DMSO-*d*₆) δ 7.59 (d, *J* = 9.0 Hz, 1H), 7.51 (s, 1H), 7.32–7.10 (m, 6H), 4.66 (t, *J* = 5.5 Hz, 1H), 4.52 (ddd, *J* = 15.2, 10.8, 4.3 Hz, 1H), 3.99–3.90 (m, 1H), 3.80–3.75 (m, 1H), 3.41–3.28 (m, 1H), 3.28–3.18 (m, 1H), 3.14 (t, *J* = 8.9 Hz, 1H), 3.10–3.00 (m, 1H), 2.29–2.20 (m, 1H), 2.20–2.09 (m, 1H), 2.03–1.98 (m, 3H), 1.81 (d, *J* = 13.0 Hz, 3H), 1.69–1.50 (m, 4H), 1.49–1.31 (m, 5H), 0.86 (dd, *J* = 8.8, 6.5 Hz, 6H).

(4-(Trifluoromethyl)cyclohexyl)methyl-((2*S*)-1-(((2*S*)-1-hydroxy-3-(2-oxopyrrolidin-3-yl)propan-2-yl)amino)-4-methyl-1-oxopentan-2-yl)carbamate (6a). Yield (83%), ¹H NMR (400 MHz, DMSO-*d*₆) δ 7.60 (d, *J* = 8.9 Hz, 1H), 7.52 (s, 1H), 7.16 (d, *J* = 8.3 Hz, 1H), 4.66 (s, 1H), 3.99–3.89 (m, 1H), 3.83–3.71 (m, 2H), 3.27–3.19 (m, 2H), 3.15 (t, 2H), 3.10–3.02 (m, 1H), 2.26–2.08 (m, 3H), 1.91–1.73 (m, 4H), 1.64–1.52 (m, 4H), 1.49–1.31 (m, 1H), 1.30–1.15 (m, 1H), 1.08–0.94 (m, 4H), 0.90–0.81 (m, 6H).

(1*r*,4*S*)-4-(Trifluoromethyl)cyclohexylmethyl-((2*S*)-1-(((2*S*)-1-hydroxy-3-(2-oxopyrrolidin-3-yl)propan-2-yl)amino)-4-methyl-1-oxopentan-2-yl)carbamate (7a). Yield (80%), ¹H NMR (400 MHz, DMSO-*d*₆) δ 7.61 (d, *J* = 9.0 Hz, 1H), 7.53 (s, 1H), 7.19 (d, *J* = 8.2 Hz, 1H), 4.67 (s, 2H), 4.07–3.86 (m, 2H), 3.76 (s, 1H), 3.26–3.18 (m, 1H), 3.17–3.11 (m, 2H), 3.09–3.01 (m, 2H), 2.33–2.19 (m, 3H), 2.18–2.09 (m, 1H), 1.89–1.85 (m, 2H), 1.84–1.72 (m, 2H), 1.64–1.32 (m, 9H), 0.90–0.81 (m, 6H).

(1*r*,4*R*)-4-Propylcyclohexylmethyl-((2*S*)-1-(((2*S*)-1-hydroxy-3-(2-oxopyrrolidin-3-yl)propan-2-yl)amino)-4-methyl-1-oxopentan-2-yl)carbamate (8a). Yield (86%), ¹H NMR (400 MHz, DMSO-*d*₆) δ 7.62–7.57 (m, 1H), 7.52 (s, 1H), 7.12 (d, *J* = 8.3 Hz, 1H), 4.65 (s, 1H), 3.99–3.89 (m, 1H), 3.82–3.68 (m, 3H), 3.37–3.19 (m, 2H), 3.18–3.02 (m, 2H), 2.26–2.07 (m, 4H), 1.76–1.65 (m, 4H), 1.62–1.51 (m, 8H), 1.49–1.32 (m, 2H), 1.32–1.24 (m, 2H), 1.21–1.10 (m, 2H), 0.99–0.78 (m, 9H).

(1*s*,4*S*)-4-Propylcyclohexylmethyl-*d*₂-((2*S*)-1-(((2*S*)-1-hydroxy-3-(2-oxopyrrolidin-3-yl)propan-2-yl)amino)-4-methyl-1-oxopentan-2-yl)carbamate (9a). Yield (43%), ¹H NMR (400 MHz, DMSO-*d*₆) δ 7.59 (d, *J* = 8.9 Hz, 1H), 7.52 (s, 1H), 7.12 (d, *J* = 8.3 Hz, 1H), 4.65 (s, 1H), 3.98–3.89 (m, 1H), 3.80–3.70 (m, 1H), 3.27–3.10 (m, 2H), 3.10–3.00 (m, 2H), 2.28–2.06 (m, 4H), 1.70 (s, 4H), 1.63–1.51 (m, 2H), 1.49–1.34 (m, 8H), 1.32–1.23 (m, 2H), 1.20–1.10 (m, 2H), 0.90–0.81 (m, 9H).

(4,4-Difluorocyclohexyl)methyl-((S)-1-(((S)-1-hydroxy-3-((S)-2-oxopyrrolidin-3-yl)propan-2-yl)amino)-4-methyl-1-oxopentan-2-yl)carbamate (10a). Yield (90%), ¹H NMR (400 MHz, DMSO-*d*₆) δ 7.60 (d, *J* = 8.9 Hz, 1H), 7.52 (s, 1H), 7.20 (d, *J* = 8.3 Hz, 1H), 4.66 (s, 1H), 3.95 (td, *J* = 8.9, 5.4 Hz, 1H), 3.90–3.69 (m, 3H), 3.23 (d, *J* = 5.7 Hz, 1H), 3.18–3.00 (m, 2H), 2.28–2.07 (m, 2H), 2.06–1.93 (m, 2H), 1.90–1.64 (m, 6H), 1.56 (dq, *J* = 11.9, 8.8 Hz, 2H), 1.51–1.30 (m, 3H), 1.30–1.12 (m, 2H), 0.86 (dd, *J* = 10.5, 6.6 Hz, 6H).

(4,4-Difluorocyclohexyl)methyl-*d*₂-((2*S*)-1-(((2*S*)-1-hydroxy-3-(2-oxopyrrolidin-3-yl)propan-2-yl)amino)-4-methyl-1-oxopentan-2-yl)carbamate (11a). Yield (81%), ¹H NMR (400 MHz, DMSO-*d*₆) δ 7.60 (d, *J* = 8.9 Hz, 1H), 7.52 (s, 1H), 7.20 (d, *J* = 8.2 Hz, 1H), 3.99–3.90 (m, 1H), 3.77 (s, 1H), 3.37–3.19 (m, 2H), 3.18–3.00 (m, 2H), 2.27–2.07 (m, 2H), 2.03–1.94 (m, 2H), 1.87–1.63 (m, 6H), 1.63–1.49 (m, 2H), 1.47–1.29 (m, 3H), 1.29–1.13 (m, 2H), 0.90–0.81 (m, 6H).

1-(4,4-Difluorocyclohexyl)ethyl-((S)-1-(((S)-1-hydroxy-3-((S)-2-oxopyrrolidin-3-yl)propan-2-yl)amino)-4-methyl-1-oxopentan-2-yl)carbamate (12a). Yield (76%), ¹H NMR (400 MHz, DMSO-*d*₆) δ 7.61–7.50 (m, 2H), 7.11 (d, *J* = 8.2 Hz, 1H), 4.66 (t, *J* = 5.3 Hz, 1H), 4.59–4.50 (m, 1H), 3.98–3.90 (m, 1H), 3.79–3.75 (m, 1H), 3.39–3.29 (m, 1H), 3.28–3.18 (m, 1H), 3.18–3.10 (m, 1H), 3.10–2.99 (m, 1H), 2.27–2.18 (m, 1H), 2.16–2.09 (m, 1H), 2.02–1.97 (m, 2H), 1.83–1.63 (m, 5H), 1.63–1.51 (m, 3H), 1.47–1.31 (m, 3H), 1.27–1.22 (m, 2H), 1.12 (dd, 2H), 0.90–0.81 (m, 6H).

2-(4,4-Difluorocyclohexyl)propan-2-yl-((S)-1-(((S)-1-hydroxy-3-((S)-2-oxopyrrolidin-3-yl)propan-2-yl)amino)-4-methyl-1-oxopentan-2-yl)carbamate (**13a**). Yield (72%). ^1H NMR (400 MHz, DMSO-d_6) δ 7.59–7.47 (m, 2H), 6.94 (d, $J = 8.2$ Hz, 1H), 4.66 (t, $J = 5.5$ Hz, 1H), 3.93–3.83 (m, 1H), 3.79–3.75 (m, 1H), 3.42–3.29 (m, 1H), 3.27–3.18 (m, 1H), 3.14 (t, $J = 8.9$ Hz, 1H), 3.10–2.99 (m, 1H), 2.27–2.09 (m, 2H), 2.06–1.91 (m, 3H), 1.85–1.61 (m, 5H), 1.61–1.51 (m, 2H), 1.46–1.34 (m, 3H), 1.33 (s, 6H), 1.31–1.18 (m, 2H), 0.90–0.81 (m, 6H).

1-(4,4-Difluorocyclohexyl)-2-phenylethyl-((S)-1-(((S)-1-hydroxy-3-((S)-2-oxopyrrolidin-3-yl)propan-2-yl)amino)-4-methyl-1-oxopentan-2-yl)carbamate (**14a**). Yield (79%). ^1H NMR (400 MHz, DMSO-d_6) δ 7.61–7.54 (m, 1H), 7.52 (s, 1H), 7.11 (d, $J = 8.2$ Hz, 1H), 4.66 (t, $J = 5.3$ Hz, 1H), 4.59–4.50 (m, 1H), 3.98–3.90 (m, 1H), 3.79–3.75 (m, 1H), 3.39–3.29 (m, 1H), 3.28–3.18 (m, 1H), 3.18–3.10 (m, 1H), 3.10–2.99 (m, 1H), 2.27–2.18 (m, 1H), 2.16–2.09 (m, 1H), 2.02–1.97 (m, 2H), 1.83–1.63 (m, 5H), 1.63–1.51 (m, 3H), 1.47–1.31 (m, 3H), 1.27–1.22 (m, 2H), 1.12 (dd, 3H), 0.90–0.81 (m, 6H).

(4,4-Difluorocyclohexyl)(phenyl)methyl-((S)-1-(((S)-1-hydroxy-3-((S)-2-oxopyrrolidin-3-yl)propan-2-yl)amino)-4-methyl-1-oxopentan-2-yl)carbamate (**15a**). Yield (86%). ^1H NMR (400 MHz, DMSO-d_6) δ 7.64–7.50 (m, 2H), 7.39–7.23 (m, 6H), 4.68–4.64 (m, 1H), 4.00–3.89 (m, 1H), 3.87–3.73 (m, 2H), 3.39–3.29 (m, 1H), 3.27–3.20 (m, 1H), 3.19–3.10 (m, 1H), 3.10–3.02 (m, 1H), 2.25–2.09 (m, 2H), 2.06–1.92 (m, 2H), 1.87–1.66 (m, 5H), 1.65–1.51 (m, 2H), 1.49–1.32 (m, 4H), 1.32–1.18 (m, 2H), 0.93–0.71 (m, 6H).

1-(4,4-Difluorocyclohexyl)pentyl-((S)-1-(((S)-1-hydroxy-3-((S)-2-oxopyrrolidin-3-yl)propan-2-yl)amino)-4-methyl-1-oxopentan-2-yl)carbamate (**16a**). Yield (91%). ^1H NMR (400 MHz, DMSO-d_6) δ 7.60 (d, $J = 9.0$ Hz, 1H), 7.52 (s, 1H), 7.20 (d, $J = 8.3$ Hz, 1H), 4.66 (t, $J = 5.6$ Hz, 1H), 4.00–3.90 (m, 1H), 3.90–3.77 (m, 1H), 3.77–3.74 (m, 1H), 3.40–3.31 (m, 1H), 3.29–3.19 (m, 1H), 3.14 (t, $J = 9.0$ Hz, 1H), 3.11–3.00 (m, 1H), 2.25–2.15 (m, 1H), 2.15–2.09 (m, 1H), 2.02–1.97 (m, 3H), 1.88–1.80 (m, 1H), 1.79–1.65 (m, 8H), 1.63–1.51 (m, 2H), 1.49–1.31 (m, 4H), 1.26–1.18 (m, 3H), 0.93–0.81 (m, 9H).

2-Fluorobenzyl-((S)-1-(((S)-1-hydroxy-3-((S)-2-oxopyrrolidin-3-yl)propan-2-yl)amino)-4-methyl-1-oxopentan-2-yl)carbamate (**17a**). Yield (33%). ^1H NMR (400 MHz, CDCl_3) δ 7.76 (d, $J = 7.2$ Hz, 1H), 7.42–7.34 (m, 1H), 7.34–7.27 (m, 1H), 7.12 (td, $J = 7.5, 1.2$ Hz, 1H), 7.09–7.00 (m, 1H), 6.23 (s, 1H), 5.56 (d, $J = 8.3$ Hz, 1H), 5.19–5.14 (m, 2H), 4.27–4.22 (m, 1H), 4.01–3.96 (m, 1H), 3.77–3.46 (m, 2H), 3.37–3.24 (m, 2H), 2.46–2.33 (m, 2H), 2.11–1.87 (m, 2H), 1.85–1.74 (m, 1H), 1.74–1.58 (m, 2H), 1.57–1.46 (m, 1H), 0.94 (d, $J = 5.8$ Hz, 6H).

3-Fluorobenzyl-((S)-1-(((S)-1-hydroxy-3-((S)-2-oxopyrrolidin-3-yl)propan-2-yl)amino)-4-methyl-1-oxopentan-2-yl)carbamate (**18a**). Yield (41%). ^1H NMR (400 MHz, CDCl_3) δ 7.82 (d, $J = 7.2$ Hz, 1H), 7.35–7.28 (m, 1H), 7.12–7.02 (m, 2H), 7.02–6.94 (m, 1H), 6.41 (s, 1H), 5.70 (d, $J = 8.3$ Hz, 1H), 5.16–5.00 (m, 2H), 4.29–4.22 (m, 1H), 4.02–3.93 (m, 1H), 3.74–3.53 (m, 2H), 3.36–3.22 (m, 2H), 2.45–2.30 (m, 2H), 2.07–1.95 (m, 1H), 1.79 (td, $J = 9.4, 2.8$ Hz, 1H), 1.73–1.43 (m, 4H), 0.94 (d, $J = 6.1$ Hz, 6H).

4-Fluorobenzyl-((S)-1-(((S)-1-hydroxy-3-((S)-2-oxopyrrolidin-3-yl)propan-2-yl)amino)-4-methyl-1-oxopentan-2-yl)carbamate (**19a**). Yield (37%). ^1H NMR (400 MHz, CDCl_3) δ 7.73 (d, $J = 7.4$ Hz, 1H), 7.37–7.28 (m, 2H), 7.08–6.97 (m, 2H), 6.37 (s, 1H), 5.56 (d, $J = 8.1$ Hz, 1H), 5.12–5.02 (m, 2H), 4.31–4.13 (m, 1H), 4.05–3.90 (m, 1H), 3.66–3.53 (m, 2H), 3.39–3.25 (m, 2H), 2.46–2.31 (m, 2H), 2.05–1.93 (m, 1H), 1.88–1.76 (m, 1H), 1.74–1.57 (m, 3H), 1.57–1.45 (m, 1H), 0.93 (d, $J = 6.1$ Hz, 6H).

(4-Fluorophenyl)methyl- d_2 -((S)-1-(((S)-1-hydroxy-3-((S)-2-oxopyrrolidin-3-yl)propan-2-yl)amino)-4-methyl-1-oxopentan-2-yl)carbamate (**20a**). Yield (37%). ^1H NMR (400 MHz, CDCl_3) δ 7.76 (d, $J = 7.3$ Hz, 1H), 7.36–7.29 (m, 2H), 7.07–6.98 (m, 2H), 6.32 (s, 1H), 5.55 (d, $J = 8.3$ Hz, 1H), 4.27–4.20 (m, 1H), 4.00–3.96 (m, 1H), 3.66–3.53 (m, 2H), 3.37–3.23 (m, 2H), 2.48–2.32 (m, 2H), 2.03–1.93 (m, 1H), 1.87–1.76 (m, 1H), 1.73–1.57 (m, 3H), 1.55–1.45 (m, 1H), 0.93 (d, $J = 6.1$ Hz, 6H).

(Perfluorophenyl)methyl-((2S)-1-(((2S)-1-hydroxy-3-(2-oxopyrrolidin-3-yl)propan-2-yl)amino)-4-methyl-1-oxopentan-2-yl)carbamate (**21a**). Yield (21%). ^1H NMR (400 MHz, DMSO-d_6) δ 7.66 (d, $J = 8.9$ Hz, 1H), 7.52 (s, 1H), 7.46 (d, $J = 8.0$ Hz, 1H), 5.18–

5.07 (m, 2H), 4.64 (s, 1H), 3.99–3.90 (m, 1H), 3.75 (s, 1H), 3.25–3.02 (m, 4H), 2.27–2.16 (m, 1H), 2.15–2.05 (m, 2H), 1.81–1.71 (m, 1H), 1.62–1.50 (m, 2H), 1.47–1.31 (m, 2H), 0.90–0.78 (m, 6H).

(Perfluorophenyl)methyl- d_2 -((2S)-1-(((2S)-1-hydroxy-3-(2-oxopyrrolidin-3-yl)propan-2-yl)amino)-4-methyl-1-oxopentan-2-yl)carbamate (**22a**). Yield (11%). ^1H NMR (400 MHz, DMSO-d_6) δ 7.65 (d, $J = 8.9$ Hz, 1H), 7.52 (s, 1H), 7.46 (d, $J = 8.0$ Hz, 1H), 4.64 (s, 1H), 3.99–3.90 (m, 1H), 3.75 (s, 1H), 3.25–3.02 (m, 4H), 2.26–2.16 (m, 1H), 2.15–2.05 (m, 2H), 1.81–1.71 (m, 1H), 1.60–1.49 (m, 2H), 1.46–1.31 (m, 2H), 0.90–0.77 (m, 6H).

1-Phenylbutyl-((S)-1-(((S)-1-hydroxy-3-((S)-2-oxopyrrolidin-3-yl)propan-2-yl)amino)-4-methyl-1-oxopentan-2-yl)carbamate (**23a**). Yield (60%). ^1H NMR (400 MHz, CDCl_3) δ 7.59 (dd, $J = 79.1, 7.3$ Hz, 1H), 7.36–7.21 (m, 5H), 6.24 (d, $J = 37.3$ Hz, 1H), 5.60 (t, $J = 7.1, 7.1$ Hz, 1H), 5.41 (dd, $J = 23.4, 8.0$ Hz, 1H), 4.21–4.11 (m, 1H), 4.04–3.89 (m, 1H), 3.69–3.47 (m, 2H), 3.36–3.19 (m, 2H), 2.53–2.17 (m, 2H), 2.03–1.80 (m, 3H), 1.79–1.42 (m, 3H), 1.41–1.21 (m, 2H), 0.98–0.83 (m, 11H).

1,2-Diphenylethyl-((S)-1-(((S)-1-hydroxy-3-((S)-2-oxopyrrolidin-3-yl)propan-2-yl)amino)-4-methyl-1-oxopentan-2-yl)carbamate (**24a**). Yield (83%). ^1H NMR (400 MHz, CDCl_3) δ 7.58 (dd, $J = 49.0, 7.4$ Hz, 1H), 7.33–7.16 (m, 8H), 7.11–7.02 (m, 2H), 6.09 (d, $J = 26.6$ Hz, 1H), 5.88–5.75 (m, 1H), 5.42–5.32 (m, 1H), 4.17–4.07 (m, 1H), 4.04–3.87 (m, 1H), 3.68–3.43 (m, 2H), 3.33–2.98 (m, 4H), 2.52–2.21 (m, 2H), 2.02–1.39 (m, 6H), 0.94–0.79 (m, 6H).

Preparation of Compounds 1–24b. General Procedure. To a solution of dipeptidyl alcohol **a** (1 equiv) in anhydrous dichloromethane (300 mL/g dipeptidyl alcohol) kept at 0–5 °C under a N_2 atmosphere was added Dess–Martin periodinane reagent (3.0 equiv), and the reaction mixture was stirred for 3 h at 15–20 °C. The organic phase was washed with 10% aq $\text{Na}_2\text{S}_2\text{O}_3$ (2 \times 100 mL/g dipeptidyl alcohol), followed by saturated aqueous NaHCO_3 (2 \times 100 mL/g dipeptidyl alcohol), distilled water (2 \times 100 mL/g dipeptidyl alcohol), and brine (100 mL/g dipeptidyl alcohol). The organic phase was dried over anhydrous Na_2SO_4 , filtered, and concentrated *in vacuo*. The resulting crude product was purified by flash chromatography (hexane/ethyl acetate) to yield aldehyde **b** as a white solid.

4,4-Dimethylcyclohexyl-((S)-4-methyl-1-oxo-1-(((S)-1-oxo-3-((S)-2-oxopyrrolidin-3-yl)propan-2-yl)amino)pentan-2-yl)carbamate (**1b**). Yield (80%). ^1H NMR (400 MHz, DMSO-d_6) δ 9.40 (s, 1H), 8.39 (d, $J = 7.7$ Hz, 1H), 7.62 (s, 1H), 7.19 (d, $J = 8.0$ Hz, 1H), 4.49–4.40 (m, 1H), 4.24–4.14 (m, 1H), 4.07–3.97 (m, 1H), 3.16 (t, $J = 9.2$ Hz, 1H), 3.12–3.00 (m, 1H), 2.31–2.22 (m, 1H), 2.19–2.09 (m, 1H), 1.95–1.83 (m, 1H), 1.74–1.55 (m, 5H), 1.54–1.31 (m, 6H), 1.25–1.15 (m, 2H), 0.92–0.81 (m, 12H). HRMS m/z : $[\text{M} + \text{Na}]^+$ calculated for $\text{C}_{22}\text{H}_{37}\text{N}_3\text{NaO}_5$ 446.2631; found 446.2612.

(1*R*,4*S*)-4-Isopropylcyclohexyl-((S)-4-methyl-1-oxo-1-(((S)-1-oxo-3-((S)-2-oxopyrrolidin-3-yl)propan-2-yl)amino)pentan-2-yl)carbamate (**2b**). Yield (78%). ^1H NMR (400 MHz, DMSO-d_6) δ 9.40 (s, 1H), 8.40 (d, $J = 7.6$ Hz, 1H), 7.63 (s, 1H), 7.19 (d, $J = 8.0$ Hz, 1H), 4.42–4.30 (m, 1H), 4.19 (ddd, $J = 11.4, 7.6, 4.2$ Hz, 1H), 4.07–3.96 (m, 1H), 3.28–3.01 (m, 2H), 2.35–2.19 (m, 1H), 2.19–2.08 (m, 1H), 1.95–1.84 (m, 3H), 1.73–1.57 (m, 5H), 1.53–1.36 (m, 3H), 1.27–1.20 (m, 2H), 1.02 (s, 3H), 0.97–0.80 (m, 12H). HRMS m/z : $[\text{M} + \text{Na}]^+$ calculated for $\text{C}_{23}\text{H}_{39}\text{N}_3\text{NaO}_5$ 460.2788; found 460.2777.

(1*S*,4*S*)-4-Propylcyclohexyl-((S)-4-methyl-1-oxo-1-(((S)-1-oxo-3-((S)-2-oxopyrrolidin-3-yl)propan-2-yl)amino)pentan-2-yl)carbamate (**3b**). Yield (73%). ^1H NMR (400 MHz, DMSO-d_6) δ 9.40 (s, 1H), 8.40 (d, $J = 7.7$ Hz, 1H), 7.63 (s, 1H), 7.19 (d, $J = 7.9$ Hz, 1H), 4.37 (td, $J = 11.0, 5.5$ Hz, 1H), 4.24–4.12 (m, 1H), 4.07–3.97 (m, 1H), 3.21–3.01 (m, 2H), 2.35–2.22 (m, 1H), 2.19–2.08 (m, 1H), 1.95–1.85 (m, 3H), 1.76–1.55 (m, 5H), 1.54–1.37 (m, 2H), 1.35–1.19 (m, 4H), 1.19–1.09 (m, 3H), 1.01–0.91 (m, 2H), 0.91–0.81 (m, 9H). HRMS m/z : $[\text{M} + \text{H}]^+$ calculated for $\text{C}_{23}\text{H}_{40}\text{N}_3\text{O}_5$ 438.2968; found 438.2952.

(1*S*,4*S*)-4-Butylcyclohexyl-((S)-4-methyl-1-oxo-1-(((S)-1-oxo-3-((S)-2-oxopyrrolidin-3-yl)propan-2-yl)amino)pentan-2-yl)carbamate (**4b**). Yield (65%). ^1H NMR (400 MHz, DMSO-d_6) δ 9.40 (s, 1H), 8.40 (d, $J = 7.6$ Hz, 1H), 7.63 (s, 1H), 7.19 (d, $J = 7.9$ Hz, 1H), 4.37 (td, $J = 11.0, 5.3$ Hz, 1H), 4.19 (ddd, $J = 11.5, 7.7, 4.1$ Hz, 1H), 4.02 (q, $J = 8.5$ Hz, 1H), 3.17 (t, $J = 9.1$ Hz, 1H), 3.13–3.01 (m, 1H), 2.32–

2.23 (m, 1H), 2.20–2.08 (m, 1H), 1.96–1.84 (m, 3H), 1.76–1.72 (m, 3H), 1.72–1.55 (m, 3H), 1.53–1.37 (m, 2H), 1.29–1.13 (m, 8H), 1.01–0.91 (m, 2H), 0.91–0.80 (m, 9H). HRMS m/z : $[M + Na]^+$ calculated for $C_{24}H_{41}N_3NaO_5$ 474.2944; found 474.2931.

(1*r*,4*S*)-4-Phenylcyclohexyl-((*S*)-4-methyl-1-oxo-1-(((*S*)-1-oxo-3-((*S*)-2-oxopyrrolidin-3-yl)propan-2-yl)amino)pentan-2-yl)carbamate (5b). Yield (63%). 1H NMR (400 MHz, DMSO- d_6) δ 9.41 (s, 1H), 8.43 (d, $J = 7.7$ Hz, 1H), 7.63 (s, 1H), 7.32–7.10 (m, 6H), 4.53 (td, $J = 10.9, 5.4$ Hz, 1H), 4.20 (ddd, $J = 11.4, 7.5, 4.0$ Hz, 1H), 4.07–3.92 (m, 1H), 3.29–3.02 (m, 2H), 2.36–2.23 (m, 1H), 2.21–2.10 (m, 1H), 2.07–1.96 (m, 2H), 1.96–1.85 (m, 1H), 1.81 (d, $J = 12.8$ Hz, 2H), 1.70–1.56 (m, 6H), 1.56–1.42 (m, 4H), 0.89 (dd, $J = 9.5, 6.6$ Hz, 6H). HRMS m/z : $[M + Na]^+$ calculated for $C_{26}H_{37}N_3NaO_5$ 494.2631; found 494.2608.

(4-(Trifluoromethyl)cyclohexyl)methyl-((2*S*)-4-methyl-1-oxo-1-(((2*S*)-1-oxo-3-(2-oxopyrrolidin-3-yl)propan-2-yl)amino)pentan-2-yl)carbamate (6b). Yield (88%). 1H NMR (400 MHz, DMSO- d_6) δ 9.40 (s, 1H), 8.43 (d, $J = 7.6$ Hz, 1H), 7.63 (s, 1H), 7.29 (d, $J = 8.0$ Hz, 1H), 4.22–4.15 (m, 1H), 4.07–3.99 (m, 1H), 3.78 (d, $J = 2.0$ Hz, 2H), 3.20–3.05 (m, 3H), 2.31–2.08 (m, 3H), 1.95–1.76 (m, 4H), 1.70–1.40 (m, 5H), 1.29–1.16 (m, 1H), 1.02 (q, $J = 13.0$ Hz, 4H), 0.92–0.81 (m, 6H). HRMS m/z : $[M + H]^+$ calculated for $C_{22}H_{35}F_3N_3O_5$ 478.2529; found 478.2522. HRMS m/z : $[M + Na]^+$ calculated for $C_{22}H_{34}F_3N_3NaO_5$ 500.2349; found 500.2328.

(1*r*,4*S*)-4-(Trifluoromethyl)cyclohexyl)methyl-((2*S*)-4-Methyl-1-oxo-1-(((2*S*)-1-oxo-3-(2-oxopyrrolidin-3-yl)propan-2-yl)amino)pentan-2-yl)carbamate (7b). Yield (91%). 1H NMR (400 MHz, DMSO- d_6) δ 9.40 (s, 1H), 8.43 (d, $J = 7.6$ Hz, 1H), 7.63 (s, 1H), 7.31 (d, $J = 8.0$ Hz, 1H), 4.24–4.14 (m, 1H), 4.08–3.99 (m, 1H), 3.98–3.92 (m, 2H), 3.21–3.04 (m, 3H), 2.33–2.20 (m, 3H), 2.19–2.08 (m, 1H), 1.92–1.83 (m, 4H), 1.69–1.38 (m, 9H), 0.92–0.81 (m, 6H). HRMS m/z : $[M + H]^+$ calculated for $C_{22}H_{35}F_3N_3O_5$ 478.2529; found 478.2512. HRMS m/z : $[M + Na]^+$ calculated for $C_{22}H_{34}F_3N_3NaO_5$ 500.2349; found 500.2320.

(1*r*,4*R*)-4-Propylcyclohexyl)methyl-((2*S*)-4-methyl-1-oxo-1-(((2*S*)-1-oxo-3-(2-oxopyrrolidin-3-yl)propan-2-yl)amino)pentan-2-yl)carbamate (8b). Yield (42%). 1H NMR (400 MHz, DMSO- d_6) δ 9.40 (s, 1H), 8.42 (d, $J = 7.7$ Hz, 1H), 7.63 (s, 1H), 7.25 (d, $J = 8.0$ Hz, 1H), 4.22–4.15 (m, 1H), 4.05–4.01 (m, 1H), 3.78–3.74 (m, 2H), 3.20–3.05 (m, 2H), 2.19–2.10 (m, 3H), 1.94–1.85 (m, 3H), 1.75–1.60 (m, 10H), 1.54–1.40 (m, 2H), 1.33–1.23 (m, 2H), 1.17–1.10 (m, 2H), 0.97–0.81 (m, 9H). HRMS m/z : $[M + Na]^+$ calculated for $C_{24}H_{41}N_3NaO_5$ 474.2944; found 474.2013.

(1*s*,4*S*)-4-Propylcyclohexyl)methyl- d_2 -((2*S*)-4-methyl-1-oxo-1-(((2*S*)-1-oxo-3-(2-oxopyrrolidin-3-yl)propan-2-yl)amino)pentan-2-yl)carbamate (9b). Yield (96%). 1H NMR (400 MHz, DMSO- d_6) δ 9.40 (s, 1H), 8.42 (d, $J = 7.6$ Hz, 1H), 7.63 (s, 1H), 7.25 (d, $J = 8.0$ Hz, 1H), 4.24–4.14 (m, 1H), 4.08–3.97 (m, 1H), 3.21–3.03 (m, 4H), 2.31–2.10 (m, 4H), 1.75–1.67 (m, 4H), 1.55–1.35 (m, 8H), 1.35–1.22 (m, 2H), 1.18–1.10 (m, 2H), 1.00–0.76 (m, 9H). HRMS m/z : $[M + Na]^+$ calculated for $C_{24}H_{39}D_2N_3NaO_5$ 476.3070; found 476.3051.

(4,4-Difluorocyclohexyl)methyl-((*S*)-4-methyl-1-oxo-1-(((*S*)-1-oxo-3-((*S*)-2-oxopyrrolidin-3-yl)propan-2-yl)amino)pentan-2-yl)carbamate (10b). Yield (51%). 1H NMR (400 MHz, DMSO- d_6) δ 9.40 (s, 1H), 8.44 (d, $J = 7.5$ Hz, 1H), 7.95 (s, 1H), 7.36–7.28 (m, 1H), 4.19 (ddd, $J = 11.4, 7.6, 4.2$ Hz, 1H), 4.03 (td, $J = 8.8, 6.2$ Hz, 1H), 3.84 (d, $J = 6.1$ Hz, 2H), 3.24–3.02 (m, 2H), 2.37–2.08 (m, 2H), 2.08–1.94 (m, 2H), 1.94–1.80 (m, 1H), 1.80–1.55 (m, 7H), 1.55–1.33 (m, 2H), 1.33–1.11 (m, 3H), 0.97–0.79 (m, 6H). HRMS m/z : $[M + H]^+$ calculated for $C_{21}H_{34}F_2N_3O_5$ 446.2467; found 446.2452. m/z : $[M + Na]^+$ calculated for $C_{21}H_{33}F_2N_3NaO_5$ 468.2286; found 468.2281.

(4,4-Difluorocyclohexyl)methyl- d_2 -((2*S*)-4-methyl-1-oxo-1-(((2*S*)-1-oxo-3-(2-oxopyrrolidin-3-yl)propan-2-yl)amino)pentan-2-yl)carbamate (11b). Yield (63%). 1H NMR (400 MHz, DMSO- d_6) δ 9.40 (s, 1H), 8.44 (d, $J = 7.5$ Hz, 1H), 7.63 (s, 1H), 7.32 (d, $J = 8.1$ Hz, 1H), 4.23–4.15 (m, 1H), 4.07–3.99 (m, 1H), 3.21–3.05 (m, 2H), 2.32–2.20 (m, 1H), 2.19–2.10 (m, 2H), 2.05–1.95 (m, 2H), 1.79–1.58 (m, 8H), 1.55–1.40 (m, 2H), 1.30–1.15 (m, 2H), 0.92–0.83 (m, 6H). HRMS m/z : $[M + H]^+$ calculated for $C_{21}H_{32}D_2F_2N_3O_5$ 448.2592; found 448.2576. HRMS m/z : $[M + Na]^+$ calculated for $C_{21}H_{31}D_2F_2N_3NaO_5$ 470.2412; found 470.2412.

1-(4,4-Difluorocyclohexyl)ethyl-((*S*)-4-methyl-1-oxo-1-(((*S*)-1-oxo-3-((*S*)-2-oxopyrrolidin-3-yl)propan-2-yl)amino)pentan-2-yl)carbamate (12b). Yield (70%). 1H NMR (400 MHz, DMSO- d_6) δ 9.40 (s, 1H), 8.46–8.36 (m, 1H), 7.63 (s, 1H), 7.23 (d, $J = 8.2$ Hz, 1H), 4.59–4.52 (m, 1H), 4.23–4.18 (m, 1H), 4.06–3.98 (m, 1H), 3.21–3.03 (m, 2H), 2.32–2.22 (m, 1H), 2.18–2.09 (m, 1H), 2.06–1.95 (m, 3H), 1.95–1.76 (m, 2H), 1.72–1.59 (m, 5H), 1.55–1.40 (m, 2H), 1.31–1.14 (m, 3H), 1.12 (d, $J = 6.3$ Hz, 3H), 0.92–0.81 (m, 6H). HRMS m/z : $[M + Na]^+$ calculated for $C_{22}H_{35}F_2N_3NaO_5$ 482.2443; found 482.2433.

2-(4,4-Difluorocyclohexyl)propan-2-yl-((*S*)-4-methyl-1-oxo-1-(((*S*)-1-oxo-3-((*S*)-2-oxopyrrolidin-3-yl)propan-2-yl)amino)pentan-2-yl)carbamate (13b). Yield (42%). 1H NMR (400 MHz, DMSO- d_6) δ 9.40 (s, 1H), 8.35 (d, $J = 7.7$ Hz, 1H), 7.70–7.60 (m, 1H), 7.06 (d, $J = 8.1$ Hz, 1H), 4.02–3.89 (m, 2H), 3.21–3.00 (m, 2H), 2.31–2.11 (m, 1H), 2.07–1.83 (m, 4H), 1.82–1.74 (m, 4H), 1.69–1.58 (m, 4H), 1.56–1.36 (m, 3H), 1.34 (s, 6H), 1.30–1.23 (m, 1H), 0.92–0.81 (m, 6H). HRMS m/z : $[M + Na]^+$ calculated for $C_{23}H_{38}F_2N_3O_5$ 474.2779; found 474.2771.

1-(4,4-Difluorocyclohexyl)-2-phenylethyl-((*S*)-4-methyl-1-oxo-1-(((*S*)-1-oxo-3-((*S*)-2-oxopyrrolidin-3-yl)propan-2-yl)amino)pentan-2-yl)carbamate (14b). Yield (80%). 1H NMR (400 MHz, DMSO- d_6) δ 9.39 (s, 1H), 8.38–8.30 (m, 1H), 7.62 (s, 1H), 7.26–7.15 (m, 5H), 4.77–4.73 (m, 1H), 4.22–4.18 (m, 1H), 3.93–3.87 (m, 1H), 3.18–2.99 (m, 2H), 2.92–2.83 (m, 1H), 2.78–2.68 (m, 1H), 2.32–2.18 (m, 1H), 2.16–2.07 (m, 1H), 2.07–1.94 (m, 2H), 1.91–1.80 (m, 3H), 1.79–1.68 (m, 1H), 1.67–1.41 (m, 7H), 1.41–1.27 (m, 3H), 0.92–0.80 (m, 4H), 0.75 (dd, $J = 11.6, 6.5$ Hz, 2H). HRMS m/z : $[M + Na]^+$ calculated for $C_{28}H_{36}F_2N_3NaO_5$ 558.2756; found 558.2740.

(4,4-Difluorocyclohexyl)(phenyl)methyl-((*S*)-4-Methyl-1-oxo-1-(((*S*)-1-oxo-3-((*S*)-2-oxopyrrolidin-3-yl)propan-2-yl)amino)pentan-2-yl)carbamate (15b). Yield (63%). 1H NMR (400 MHz, DMSO- d_6) δ 9.41 (s, 1H), 8.48–8.35 (m, 1H), 7.65 (d, $J = 5.4$ Hz, 1H), 7.52–7.43 (m, 1H), 7.39–7.20 (m, 5H), 4.22–4.17 (m, 1H), 4.00–3.96 (m, 1H), 3.85 (d, $J = 6.0$ Hz, 1H), 3.23–3.05 (m, 2H), 2.32–2.22 (m, 1H), 2.17–2.13 (m, 1H), 2.05–1.87 (m, 3H), 1.84–1.72 (m, 2H), 1.70–1.59 (m, 4H), 1.55–1.38 (m, 3H), 1.33–1.16 (m, 3H), 0.97–0.74 (m, 6H). HRMS m/z : $[M + Na]^+$ calculated for $C_{27}H_{37}F_2N_3NaO_5$ 544.2599; found 544.2586.

1-(4,4-Difluorocyclohexyl)pentyl-((*S*)-4-methyl-1-oxo-1-(((*S*)-1-oxo-3-((*S*)-2-oxopyrrolidin-3-yl)propan-2-yl)amino)pentan-2-yl)carbamate (16b). Yield (88%). 1H NMR (400 MHz, DMSO- d_6) δ 9.40 (s, 1H), 8.43 (d, $J = 7.6$ Hz, 1H), 7.63 (s, 1H), 7.32 (d, $J = 8.0$ Hz, 1H), 4.24–4.14 (m, 1H), 4.05–4.00 (m, 1H), 3.87–3.81 (m, 1H), 3.21–3.04 (m, 2H), 2.30–2.22 (m, 1H), 2.19–2.08 (m, 1H), 2.06–1.94 (m, 3H), 1.94–1.80 (m, 3H), 1.79–1.71 (m, 5H), 1.69–1.58 (m, 4H), 1.55–1.41 (m, 3H), 1.26–1.18 (m, 3H), 0.92–0.81 (m, 9H). HRMS m/z : $[M + Na]^+$ calculated for $C_{25}H_{41}F_2N_3NaO_5$ 524.2912; found 524.2888.

2-Fluorobenzyl-((*S*)-4-methyl-1-oxo-1-(((*S*)-1-oxo-3-((*S*)-2-oxopyrrolidin-3-yl)propan-2-yl)amino)pentan-2-yl)carbamate (17b). Yield (68%). 1H NMR (400 MHz, CDCl $_3$) δ 9.48 (s, 1H), 8.35 (d, $J = 5.9$ Hz, 1H), 7.39 (t, $J = 7.6$ Hz, 1H), 7.35–7.27 (m, 1H), 7.18–7.00 (m, 2H), 6.02 (s, 1H), 5.38 (d, $J = 8.5$ Hz, 1H), 5.22–5.16 (m, 2H), 4.44–4.26 (m, 2H), 3.39–3.27 (m, 2H), 2.49–2.30 (m, 2H), 2.01–1.92 (m, 2H), 1.91–1.80 (m, 1H), 1.81–1.45 (m, 3H), 0.97 (d, $J = 5.8$ Hz, 6H). HRMS m/z : $[M + Na]^+$ calculated for $C_{21}H_{28}FN_3NaO_5$: 444.1911, found: 444.1907.

3-Fluorobenzyl-((*S*)-4-methyl-1-oxo-1-(((*S*)-1-oxo-3-((*S*)-2-oxopyrrolidin-3-yl)propan-2-yl)amino)pentan-2-yl)carbamate (18b). Yield (68%). 1H NMR (400 MHz, CDCl $_3$) δ 9.48 (s, 1H), 8.45 (d, $J = 5.7$ Hz, 1H), 7.35–7.24 (m, 1H), 7.13–7.05 (m, 2H), 7.05–6.94 (m, 1H), 6.18 (s, 1H), 5.48 (d, $J = 8.6$ Hz, 1H), 5.16–5.03 (m, 2H), 4.41–4.26 (m, 2H), 3.41–3.27 (m, 2H), 2.56–2.29 (m, 2H), 2.00–1.79 (m, 2H), 1.77–1.64 (m, 3H), 1.60–1.51 (m, 1H), 0.97 (d, $J = 6.0$ Hz, 6H). HRMS m/z : $[M + Na]^+$ calculated for $C_{21}H_{28}FN_3NaO_5$: 444.1911, found: 444.1911.

4-Fluorobenzyl-((*S*)-4-methyl-1-oxo-1-(((*S*)-1-oxo-3-((*S*)-2-oxopyrrolidin-3-yl)propan-2-yl)amino)pentan-2-yl)carbamate (19b). Yield (60%). 1H NMR (400 MHz, CDCl $_3$) δ 9.48 (s, 1H), 8.36 (d, $J = 5.7$ Hz, 1H), 7.38–7.29 (m, 2H), 7.09–6.98 (m, 2H), 6.00 (s, 1H),

5.36 (d, $J = 8.6$ Hz, 1H), 5.11–5.04 (m, 2H), 4.35–4.28 (m, 2H), 3.41–3.28 (m, 2H), 2.50–2.31 (m, 2H), 1.97–1.93 (m, 1H), 1.90–1.76 (m, 1H), 1.74–1.65 (m, 3H), 1.59–1.51 (m, 1H), 0.96 (d, $J = 6.0$ Hz, 6H). HRMS m/z : $[M + H]^+$ calculated for $C_{21}H_{29}FN_3O_5$: 422.2091, found: 422.2085. HRMS m/z : $[M + Na]^+$ calculated for $C_{21}H_{28}FN_3NaO_5$: 444.1911, found: 444.1903.

(4-Fluorophenyl)methyl-*d*-((*S*)-4-methyl-1-oxo-1-(((*S*)-1-oxo-3-((*S*)-2-oxopyrrolidin-3-yl)propan-2-yl)amino)pentan-2-yl)carbamate (20b). Yield (75%). 1H NMR (400 MHz, $CDCl_3$) δ 9.48 (s, 1H), 8.36 (d, $J = 5.7$ Hz, 1H), 7.37–7.28 (m, 2H), 7.08–6.98 (m, 2H), 6.06 (s, 1H), 5.38 (d, $J = 8.6$ Hz, 1H), 4.39–4.14 (m, 2H), 3.41–3.30 (m, 2H), 2.48–2.29 (m, 2H), 2.01–1.92 (m, 1H), 1.92–1.80 (m, 1H), 1.80–1.62 (m, 3H), 1.59–1.46 (m, 1H), 0.96 (d, $J = 5.9$ Hz, 6H). HRMS m/z : $[M + H]^+$ calculated for $C_{21}H_{27}D_2FN_3O_5$: 424.2217, found: 424.2210. HRMS m/z : $[M + Na]^+$ calculated for $C_{21}H_{26}D_2FN_3NaO_5$: 446.2037, found: 446.2027.

(Perfluorophenyl)methyl-((2*S*)-4-methyl-1-oxo-1-(((2*S*)-1-oxo-3-(2-oxopyrrolidin-3-yl)propan-2-yl)amino)pentan-2-yl)carbamate (21b). Yield (86%). 1H NMR (400 MHz, $DMSO-d_6$) δ 9.39 (s, 1H), 8.47 (d, $J = 7.5$ Hz, 1H), 7.63 (s, 1H), 7.59 (d, $J = 7.8$ Hz, 1H), 5.14 (s, 2H), 4.23–4.14 (m, 1H), 4.07–3.98 (m, 1H), 3.22–3.03 (m, 2H), 2.33–2.20 (m, 1H), 2.17–2.06 (m, 2H), 1.93–1.83 (m, 1H), 1.70–1.56 (m, 2H), 1.51–1.39 (m, 2H), 0.91–0.80 (m, 6H). HRMS m/z : $[M + H]^+$ calculated for $C_{21}H_{25}F_3N_3O_5$: 494.1714; found 494.1715. HRMS m/z : $[M + Na]^+$ calculated for $C_{21}H_{24}F_3N_3NaO_5$: 516.1534; found 516.1520.

(Perfluorophenyl)methyl-*d*-((2*S*)-4-Methyl-1-oxo-1-(((2*S*)-1-oxo-3-(2-oxopyrrolidin-3-yl)propan-2-yl)amino)pentan-2-yl)carbamate (22b). Yield (83%). 1H NMR (400 MHz, $DMSO-d_6$) δ 9.38 (s, 1H), 8.46 (d, $J = 7.6$ Hz, 1H), 7.63 (s, 1H), 7.58 (d, $J = 7.8$ Hz, 1H), 4.22–4.14 (m, 1H), 4.06–3.99 (m, 1H), 3.20–3.05 (m, 2H), 2.27 (d, $J = 7.9$ Hz, 1H), 2.16–2.07 (m, 2H), 1.92–1.83 (m, 1H), 1.68–1.58 (m, 2H), 1.50–1.41 (m, 2H), 0.90–0.80 (m, 6H). HRMS m/z : $[M + H]^+$ calculated for $C_{21}H_{23}D_2F_3N_3O_5$: 496.1840; found 496.1837. HRMS m/z : $[M + Na]^+$ calculated for $C_{21}H_{22}D_2F_3N_3NaO_5$: 518.1660; found 518.1646.

1-Phenylbutyl-((*S*)-4-Methyl-1-oxo-1-(((*S*)-1-oxo-3-((*S*)-2-oxopyrrolidin-3-yl)propan-2-yl)amino)pentan-2-yl)carbamate (23b). Yield (71%). 1H NMR (400 MHz, $CDCl_3$) δ 9.44 (d, $J = 36.5$ Hz, 1H), 8.21 (dd, $J = 43.6, 6.1$ Hz, 1H), 7.41–7.17 (m, 5H), 6.28 (d, $J = 30.3$ Hz, 1H), 5.68–5.54 (m, 1H), 5.36 (dd, $J = 26.5, 8.5$ Hz, 1H), 4.40–4.19 (m, 2H), 3.41–3.15 (m, 2H), 2.56–2.14 (m, 2H), 2.01–1.81 (m, 3H), 1.77–1.62 (m, 3H), 1.59–1.44 (m, 1H), 1.42–1.25 (m, 1H), 1.00–0.77 (m, 11H). HRMS m/z : $[M + Na]^+$ calculated for $C_{24}H_{35}N_3NaO_5$: 468.2475; found 468.2463.

1,2-Diphenylethyl-((*S*)-4-Methyl-1-oxo-1-(((*S*)-1-oxo-3-((*S*)-2-oxopyrrolidin-3-yl)propan-2-yl)amino)pentan-2-yl)carbamate (24b). Yield (82%). 1H NMR (400 MHz, $DMSO-d_6$) δ 9.35 (dd, $J = 24.5, 7.6$ Hz, 1H), 8.48–8.32 (m, 1H), 7.61 (d, $J = 21.6$ Hz, 1H), 7.53–7.42 (m, 1H), 7.36–7.09 (m, 10H), 5.83–5.71 (m, 1H), 4.24–4.08 (m, 1H), 4.06–3.89 (m, 1H), 3.24–2.86 (m, 4H), 2.34–2.05 (m, 3H), 1.94–1.78 (m, 1H), 1.67–1.28 (m, 4H), 0.90–0.68 (m, 6H). HRMS m/z : $[M + Na]^+$ calculated for $C_{28}H_{35}N_3NaO_5$: 516.2475; found 516.2462.

Preparation of Compounds 1–24c. General Procedure. To a solution of dipeptidyl aldehyde **b** (1 equiv) in ethyl acetate (10 mL/g of dipeptidyl aldehyde) was added absolute ethanol (5 mL/g of dipeptidyl aldehyde) with stirring, followed by a solution of sodium bisulfite (1 equiv) in water (1 mL/g of dipeptidyl aldehyde). The reaction mixture was stirred for 3 h at 50 °C. The reaction mixture was allowed to cool to room temperature and then vacuum-filtered. The solid was thoroughly washed with absolute ethanol, and the filtrate was dried over anhydrous sodium sulfate, filtered, and concentrated to yield a white solid. The white solid was stirred with dry ethyl ether (3 \times 10 mL/g of dipeptidyl aldehyde), followed by careful removal of the solvent using a pipette and dried using a vacuum pump for 2 h to yield dipeptidyl bisulfite adduct **c** as a white solid.

Sodium-(2*S*)-2-((*S*)-2-(((4,4-dimethylcyclohexyl)oxy)carbonyl)amino)-4-methylpentanamido)-1-hydroxy-3-((*S*)-2-oxopyrrolidin-3-yl)propane-1-sulfonate (1c). Yield (39%). 1H NMR (400 MHz, $DMSO-d_6$) δ 7.50 (dd, $J = 13.4, 9.1$ Hz, 1H), 7.44 (s, 1H), 7.21–7.11

(m, 1H), 5.45–5.27 (m, 1H), 4.53–4.39 (m, 1H), 4.01–3.92 (m, 1H), 3.95–3.78 (m, 1H), 3.14–3.08 (m, 1H), 3.06–3.01 (m, 1H), 2.19–2.05 (m, 1H), 2.04–1.86 (m, 1H), 1.70–1.65 (m, 3H), 1.62–1.52 (m, 3H), 1.52–1.31 (m, 6H), 1.28–1.09 (m, 2H), 0.92–0.80 (m, 12H). HRMS m/z : $[M + Na]^+$ calculated for $C_{22}H_{38}N_3Na_2O_8S$: 550.2175; found 550.2154.

Sodium-(2*S*)-1-hydroxy-2-((*S*)-2-(((1*r*,4*S*)-4-isopropylcyclohexyl)oxy)carbonyl)amino)-4-methylpentanamido)-3-((*S*)-2-oxopyrrolidin-3-yl)propane-1-sulfonate (2c). Yield (36%). 1H NMR (400 MHz, $DMSO-d_6$) δ 7.54–7.42 (m, 2H), 7.23–7.11 (m, 1H), 5.45–5.28 (m, 1H), 4.41–4.30 (m, 1H), 4.00–3.89 (m, 1H), 3.89–3.78 (m, 1H), 3.17–3.09 (m, 1H), 3.08–2.97 (m, 1H), 2.14–2.04 (m, 2H), 2.01–1.84 (m, 3H), 1.73–1.65 (m, 2H), 1.62–1.51 (m, 3H), 1.48–1.34 (m, 3H), 1.30–1.14 (m, 2H), 1.01 (s, 3H), 0.89–0.80 (m, 12H). HRMS m/z : $[M + Na]^+$ calculated for $C_{23}H_{40}N_3Na_2O_8S$: 564.2332; found 564.2450.

Sodium-(2*S*)-1-hydroxy-2-((*S*)-4-methyl-2-(((1*s*,4*S*)-4-propylcyclohexyl)oxy)carbonyl)amino)pentanamido)-3-((*S*)-2-oxopyrrolidin-3-yl)propane-1-sulfonate (3c). Yield (40%). 1H NMR (400 MHz, $DMSO-d_6$) δ 7.54–7.39 (m, 2H), 7.23–7.10 (m, 1H), 5.45–5.28 (m, 1H), 4.42–4.32 (m, 1H), 4.03–3.88 (m, 1H), 3.89–3.78 (m, 1H), 3.18–3.08 (m, 1H), 3.07–2.97 (m, 1H), 2.19–2.03 (m, 2H), 1.97–1.80 (m, 3H), 1.71 (d, $J = 13.2$ Hz, 2H), 1.59–1.56 (m, 3H), 1.48–1.37 (m, 2H), 1.34–1.02 (m, 7H), 0.97–0.89 (m, 2H), 0.92–0.80 (m, 9H). HRMS m/z : $[M + Na]^+$ calculated for $C_{23}H_{40}N_3Na_2O_8S$: 564.2332; found 564.2311.

Sodium-(2*S*)-2-((*S*)-2-(((1*s*,4*S*)-4-butylcyclohexyl)oxy)carbonyl)amino)-4-methylpentanamido)-1-hydroxy-3-((*S*)-2-oxopyrrolidin-3-yl)propane-1-sulfonate (4c). Yield (33%). 1H NMR (400 MHz, $DMSO-d_6$) δ 7.55–7.42 (m, 2H), 7.22–7.12 (m, 1H), 5.48–5.30 (m, 1H), 4.42–4.32 (m, 1H), 3.97–3.89 (m, 1H), 3.88–3.79 (m, 1H), 3.17–3.08 (m, 1H), 3.07–2.98 (m, 1H), 2.19–2.02 (m, 2H), 1.99–1.83 (m, 3H), 1.72 (d, $J = 13.3$ Hz, 3H), 1.60–1.55 (m, 3H), 1.48–1.37 (m, 2H), 1.27–1.17 (m, 6H), 1.17–1.13 (m, 3H), 0.97–0.92 (m, 1H), 0.90–0.80 (m, 9H). HRMS m/z : $[M + Na]^+$ calculated for $C_{24}H_{42}N_3Na_2O_8S$: 578.2488; found 578.2473.

Sodium-(2*S*)-1-hydroxy-2-((*S*)-4-methyl-2-(((1*r*,4*S*)-4-phenylcyclohexyl)oxy)carbonyl)amino)pentanamido)-3-((*S*)-2-oxopyrrolidin-3-yl)propane-1-sulfonate (5c). Yield (35%). 1H NMR (400 MHz, $DMSO-d_6$) δ 7.57–7.47 (m, 1H), 7.44 (s, 1H), 7.32–7.10 (m, 6H), 5.52–5.22 (m, 1H), 4.55–4.50 (m, 1H), 4.06–3.89 (m, 1H), 3.89–3.77 (m, 1H), 3.15–3.10 (m, 1H), 3.09–3.00 (m, 1H), 2.14–2.09 (m, 2H), 2.05–1.97 (m, 2H), 1.81 (d, $J = 13.1$ Hz, 3H), 1.62–1.52 (m, 5H), 1.50–1.39 (m, 4H), 1.14–1.03 (m, 1H), 0.93–0.81 (m, 6H). HRMS m/z : $[M + Na]^+$ calculated for $C_{26}H_{38}N_3Na_2O_8S$: 598.2175; found 598.2152.

Sodium-(2*S*)-1-hydroxy-2-((*S*)-4-methyl-2-(((4-(trifluoromethyl)cyclohexyl)methoxy)carbonyl)amino)pentanamido)-3-(2-oxopyrrolidin-3-yl)propane-1-sulfonate (6c). Yield (81%). 1H NMR (400 MHz, $DMSO-d_6$) δ 7.62–7.49 (m, 1H), 7.46 (s, 1H), 7.25–7.13 (m, 1H), 5.50 (d, $J = 6.3$ Hz, 1H), 5.34 (d, $J = 6.0$ Hz, 1H), 4.41–4.33 (m, 1H), 4.27–4.18 (m, 1H), 3.81–3.70 (m, 2H), 3.13 (s, 2H), 3.08–2.99 (m, 1H), 2.20–2.06 (m, 3H), 1.91–1.76 (m, 4H), 1.63–1.57 (m, 4H), 1.49–1.37 (m, 1H), 1.27–1.16 (m, 1H), 1.13–0.92 (m, 4H), 0.93–0.80 (m, 6H). HRMS m/z : $[M + Na]^+$ calculated for $C_{22}H_{35}F_3N_3Na_2O_8S$: 604.1893; found 604.1871.

Sodium-(2*S*)-1-hydroxy-2-((*S*)-4-methyl-2-(((1*r*,4*S*)-4-(trifluoromethyl)cyclohexyl)methoxy)carbonyl)amino)pentanamido)-3-(2-oxopyrrolidin-3-yl)propane-1-sulfonate (7c). Yield (76%). 1H NMR (400 MHz, $DMSO-d_6$) δ 7.58–7.50 (m, 1H), 7.46 (d, $J = 9.6$ Hz, 1H), 7.25–7.16 (m, 1H), 5.41 (d, $J = 6.3$ Hz, 1H), 5.28 (d, $J = 5.9$ Hz, 1H), 4.45–4.32 (m, 1H), 4.00–3.90 (m, 2H), 3.50–3.25 (m, 1H), 3.08–3.01 (m, 2H), 2.31–2.26 (m, 3H), 2.15–2.08 (m, 1H), 1.90–1.85 (m, 4H), 1.67–1.33 (m, 10H), 0.91–0.81 (m, 6H). HRMS m/z : $[M + Na]^+$ calculated for $C_{22}H_{35}F_3N_3Na_2O_8S$: 604.1893; found 604.1862.

Sodium-(2*S*)-1-hydroxy-2-((*S*)-4-methyl-2-(((1*r*,4*R*)-4-propylcyclohexyl)methoxy)carbonyl)amino)pentanamido)-3-(2-oxopyrrolidin-3-yl)propane-1-sulfonate (8c). Yield (82%). 1H NMR (400 MHz, $DMSO-d_6$) δ 7.53–7.40 (m, 1H), 7.20–7.09 (m, 1H), 6.10–6.04 (m, 1H), 5.41 (d, $J = 6.2$ Hz, 1H), 5.29 (d, $J = 6.30$ Hz, 1H),

4.43–4.32 (m, 1H), 4.00–3.89 (m, 1H), 3.74 (s, 2H), 3.16–3.01 (m, 2H), 2.15–2.05 (m, 6H), 1.71 (d, $J = 11.4$ Hz, 10H), 1.53–1.36 (m, 2H), 1.35–1.22 (m, 2H), 1.19–1.03 (m, 2H), 0.98–0.77 (m, 9H). HRMS m/z : $[M + Na]^+$ calculated for $C_{24}H_{42}N_3Na_2O_8S$ 578.2488; found 578.2460.

Sodium-(2S)-1-hydroxy-2-(((S)-4-methyl-2-((((1S,4S)-4-propylcyclohexyl)methoxy- d_2)carbonyl)amino)pentanamido)-3-(2-oxopyrrolidin-3-yl)propane-1-sulfonate (9c). Yield (77%). 1H NMR (400 MHz, DMSO- d_6) δ 7.57–7.42 (m, 1H), 7.27–7.09 (m, 1H), 6.07 (d, $J = 10.0$ Hz, 1H), 5.40 (d, $J = 6.4$ Hz, 1H), 5.29 (d, $J = 6.0$ Hz, 1H), 3.99–3.89 (m, 1H), 3.78–3.69 (m, 1H), 3.17–2.98 (m, 4H), 2.20–2.06 (m, 4H), 1.71 (d, $J = 11.6$ Hz, 4H), 1.49–1.35 (m, 8H), 1.35–1.22 (m, 2H), 1.18–1.09 (m, 2H), 0.90–0.80 (m, 2H). HRMS m/z : $[M + Na]^+$ calculated for $C_{24}H_{40}D_2N_3Na_2O_8S$ 580.2614; found 580.2582.

Sodium-(2S)-2-(((S)-2-((((4,4-difluorocyclohexyl)methoxy)carbonyl)amino)-4-methylpentanamido)-1-hydroxy-3-(((S)-2-oxopyrrolidin-3-yl)propane-1-sulfonate (10c). Yield (50.5%). 1H NMR (400 MHz, DMSO- d_6) δ 7.57 (t, $J = 8.9$ Hz, 1H), 7.45 (s, 1H), 7.38–7.17 (m, 1H), 4.29–4.10 (m, 1H), 4.05–3.67 (m, 4H), 3.09 (dt, $J = 29.8, 8.8$ Hz, 2H), 2.33–2.05 (m, 2H), 2.05–1.88 (m, 4H), 1.88–1.64 (m, 5H), 1.64–1.48 (m, 2H), 1.43 (q, $J = 7.3$ Hz, 2H), 1.30–1.11 (m, 2H), 1.04–0.78 (m, 6H).

Sodium-(2S)-2-(((S)-2-((((4,4-difluorocyclohexyl)methoxy- d_2)carbonyl)amino)-4-methylpentanamido)-1-hydroxy-3-(2-oxopyrrolidin-3-yl)propane-1-sulfonate (11c). Yield (81%). 1H NMR (400 MHz, DMSO- d_6) δ 7.60–7.50 (m, 1H), 7.45 (s, 1H), 7.29–7.18 (m, 1H), 5.41 (d, $J = 6.3$ Hz, 1H), 5.24 (d, $J = 6.0$ Hz, 1H), 4.37–4.32 (m, 1H), 3.98–3.89 (m, 1H), 3.15–3.02 (m, 2H), 2.14–2.05 (m, 3H), 2.01–1.96 (m, 1H), 1.84–1.70 (m, 8H), 1.62–1.53 (m, 4H), 1.45–1.38 (m, 1H), 0.90–0.80 (m, 6H). HRMS m/z : $[M + Na]^+$ calculated for $C_{21}H_{32}D_2F_2N_3Na_2O_8S$ 574.1956; found 574.1931.

Sodium-(2S)-2-(((2S)-2-(((1-(4,4-difluorocyclohexyl)ethoxy)carbonyl)amino)-4-methylpentanamido)-1-hydroxy-3-(((S)-2-oxopyrrolidin-3-yl)propane-1-sulfonate (12c). Yield (48%). 1H NMR (400 MHz, DMSO- d_6) δ 7.52 (d, $J = 9.9$ Hz, 1H), 7.43 (s, 1H), 7.28–7.13 (m, 1H), 5.36–5.17 (m, 1H), 4.58–4.51 (m, 1H), 3.96–3.91 (m, 1H), 3.83–3.78 (m, 1H), 3.18–3.09 (m, 1H), 3.06–3.01 (m, 1H), 2.17–1.88 (m, 3H), 1.87–1.77 (m, 4H), 1.74–1.66 (m, 2H), 1.65–1.51 (m, 3H), 1.48–1.35 (m, 2H), 1.30–1.16 (m, 3H), 1.16–1.04 (m, 3H), 0.89–0.80 (m, 6H). HRMS m/z : $[M + Na]^+$ calculated for $C_{22}H_{36}F_2N_3Na_2O_8S$ 586.1987; found 586.1978.

Sodium-(2S)-2-(((S)-2-((((2-(4,4-difluorocyclohexyl)propan-2-yl)oxy)carbonyl)amino)-4-methylpentanamido)-1-hydroxy-3-(((S)-2-oxopyrrolidin-3-yl)propane-1-sulfonate (13c). Yield (39%). 1H NMR (400 MHz, DMSO- d_6) δ 7.49 (d, $J = 10.6$ Hz, 1H), 7.43 (s, 1H), 7.12–6.95 (m, 1H), 5.47–5.26 (m, 1H), 4.06–3.71 (m, 2H), 3.17–3.08 (m, 1H), 3.08–2.97 (m, 1H), 2.14–1.93 (m, 6H), 1.86–1.65 (m, 5H), 1.64–1.49 (m, 2H), 1.44–1.36 (m, 2H), 1.33 (s, 6H), 1.28–1.23 (m, 2H), 0.84 (ddd, $J = 11.6, 6.5, 3.0$ Hz, 6H). HRMS m/z : $[M + Na]^+$ calculated for $C_{23}H_{38}F_2N_3Na_2O_8S$ 600.2143; found 600.2131.

Sodium-(2S)-2-(((2S)-2-(((1-(4,4-difluorocyclohexyl)-2-phenylethoxy)carbonyl)amino)-4-methylpentanamido)-1-hydroxy-3-(((S)-2-oxopyrrolidin-3-yl)propane-1-sulfonate (14c). Yield (41%). 1H NMR (400 MHz, DMSO- d_6) δ 7.53–7.47 (m, 1H), 7.43 (s, 1H), 7.39–7.33 (m, 1H), 7.28–7.15 (m, 5H), 5.38–5.15 (m, 1H), 4.75–4.71 (m, 1H), 3.96–3.91 (m, 1H), 3.87–3.68 (m, 1H), 3.13–3.09 (m, 2H), 3.07–2.96 (m, 1H), 2.90–2.82 (m, 1H), 2.00 (s, 4H), 1.92–1.80 (m, 3H), 1.76 (s, 3H), 1.59–1.51 (m, 4H), 1.49–1.33 (m, 3H), 0.89–0.79 (m, 4H), 0.79–0.67 (m, 2H). HRMS m/z : $[M + Na]^+$ calculated for $C_{28}H_{40}F_2N_3Na_2O_8S$ 662.2300; found 662.2288.

Sodium-(2S)-2-(((2S)-2-((((4,4-difluorocyclohexyl)(phenyl)methoxy)carbonyl)amino)-4-methylpentanamido)-1-hydroxy-3-(((S)-2-oxopyrrolidin-3-yl)propane-1-sulfonate (15c). Yield (66%). 1H NMR (400 MHz, DMSO- d_6) δ 7.64–7.50 (m, 1H), 7.49–7.44 (m, 1H), 7.42–7.19 (m, 6H), 5.48–5.35 (m, 1H), 4.01–3.75 (m, 3H), 3.18–3.10 (m, 1H), 3.08–3.01 (m, 1H), 2.22–2.06 (m, 1H), 2.06–1.91 (m, 3H), 1.87–1.68 (m, 4H), 1.61–1.54 (m, 3H), 1.49–1.40 (m, 3H), 1.35–1.14 (m, 3H), 0.93–0.71 (m, 6H). HRMS m/z : $[M + Na]^+$ calculated for $C_{27}H_{38}F_2N_3Na_2O_8S$ 648.2143; found 648.2121.

Sodium-(2S)-2-(((2S)-2-((((1-(4,4-difluorocyclohexyl)pentyl)oxy)carbonyl)amino)-4-methylpentanamido)-1-hydroxy-3-(((S)-2-oxo-

pyrrolidin-3-yl)propane-1-sulfonate (16c). Yield (58%). 1H NMR (400 MHz, DMSO- d_6) δ 7.60–7.51 (m, 1H), 7.44 (s, 1H), 7.38–7.23 (m, 1H), 5.46–5.21 (m, 1H), 3.98–3.74 (m, 3H), 3.14–3.07 (m, 1H), 3.06–2.98 (m, 1H), 2.16–2.04 (m, 2H), 2.04–1.92 (m, 4H), 1.86–1.66 (m, 8H), 1.64–1.52 (m, 3H), 1.49–1.36 (m, 3H), 1.21–1.17 (m, 3H), 0.83 (ddd, $J = 11.9, 6.5, 3.1$ Hz, 9H). HRMS m/z : $[M + Na]^+$ calculated for $C_{25}H_{42}F_2N_3Na_2O_8S$ 628.2456; found 628.2419.

Sodium-(2S)-2-(((S)-2-((((2-fluorobenzyl)oxy)carbonyl)amino)-4-methylpentanamido)-1-hydroxy-3-(((S)-2-oxopyrrolidin-3-yl)propane-1-sulfonate (17c). Yield (71%). 1H NMR (400 MHz, DMSO- d_6) δ 7.77–7.70 (m, 1H), 7.70–7.59 (m, 1H), 7.59–7.33 (m, 3H), 7.26–7.12 (m, 2H), 5.65 (d, $J = 78.6$ Hz, 1H), 5.16–5.01 (m, 2H), 4.11–3.84 (m, 2H), 3.17–2.97 (m, 2H), 2.39–2.07 (m, 2H), 2.07–1.85 (m, 1H), 1.70–1.51 (m, 3H), 1.51–1.33 (m, 2H), 0.92–0.77 (m, 6H). HRMS m/z : $[M]^+$ calculated for $C_{21}H_{29}FN_3O_8S$: 502.1659, found: 502.1650. HRMS m/z : $[M + Na]^+$ calculated for $C_{21}H_{29}FN_3Na_2O_8S$: 548.1455, found: 548.1446.

Sodium-(2S)-2-(((S)-2-((((3-fluorobenzyl)oxy)carbonyl)amino)-4-methylpentanamido)-1-hydroxy-3-(((S)-2-oxopyrrolidin-3-yl)propane-1-sulfonate (18c). Yield (89%). 1H NMR (400 MHz, DMSO- d_6) δ 7.75 (d, $J = 9.0$ Hz, 1H), 7.64 (d, $J = 9.3$ Hz, 1H), 7.57 (d, $J = 7.9$ Hz, 1H), 7.54–7.35 (m, 2H), 7.25–7.08 (m, 2H), 5.75–5.46 (m, 1H), 5.15–4.98 (m, 2H), 4.13–3.87 (m, 2H), 3.17–2.89 (m, 2H), 2.23–2.04 (m, 2H), 2.04–1.91 (m, 1H), 1.89–1.74 (m, 1H), 1.70–1.31 (m, 4H), 0.91–0.77 (m, 6H). HRMS m/z : $[M + Na]^+$ calculated for $C_{21}H_{29}FN_3Na_2O_8S$: 548.1455, found: 548.1450. HRMS m/z : $[M]^+$ calculated for $C_{21}H_{29}FN_3O_8S$: 502.1659, found: 502.1655.

Sodium-(2S)-2-(((S)-2-((((4-fluorobenzyl)oxy)carbonyl)amino)-4-methylpentanamido)-1-hydroxy-3-(((S)-2-oxopyrrolidin-3-yl)propane-1-sulfonate (19c). Yield (68%). 1H NMR (400 MHz, DMSO- d_6) δ 7.70–7.57 (m, 1H), 7.57–7.49 (m, 1H), 7.48–7.37 (m, 3H), 7.23–7.14 (m, 2H), 5.43 (d, $J = 85.6$ Hz, 1H), 5.09–4.92 (m, 2H), 4.12–3.81 (m, 2H), 3.14–2.94 (m, 2H), 2.23–1.91 (m, 2H), 1.62–1.50 (m, 4H), 1.50–1.38 (m, 2H), 0.90–0.80 (m, 6H). HRMS m/z : $[M + Na]^+$ calculated for $C_{21}H_{29}FN_3Na_2O_8S$: 548.1455, found: 548.1448. HRMS m/z : $[M]^+$ calculated for $C_{21}H_{29}FN_3O_8S$: 502.1659, found: 502.1645.

Sodium-(2S)-2-(((S)-2-((((4-fluorophenyl)methoxy- d_2)carbonyl)amino)-4-methylpentanamido)-1-hydroxy-3-(((S)-2-oxopyrrolidin-3-yl)propane-1-sulfonate (20c). Yield (90%). 1H NMR (400 MHz, DMSO- d_6) δ 7.68 (d, $J = 9.2$ Hz, 1H), 7.63 (d, $J = 9.2$ Hz, 1H), 7.53 (d, $J = 7.8$ Hz, 1H), 7.48–7.35 (m, 2H), 7.23–7.13 (m, 2H), 5.52 (dd, $J = 85.5, 6.2$ Hz, 1H), 4.04–3.84 (m, 2H), 3.18–2.97 (m, 2H), 2.27–1.90 (m, 2H), 1.63–1.50 (m, 3H), 1.53–1.38 (m, 3H), 0.92–0.78 (m, 6H). HRMS m/z : $[M + Na]^+$ calculated for $C_{21}H_{27}D_2FN_3Na_2O_8S$: 550.1581, found: 550.1573. HRMS m/z : $[M + Na]^+$ calculated for $C_{21}H_{27}D_2FN_3O_8S$: 504.1785, found: 504.1769.

Sodium-(2S)-1-hydroxy-2-(((S)-4-methyl-2-(((perfluorophenyl)methoxy)carbonyl)amino)pentanamido)-3-(2-oxopyrrolidin-3-yl)propane-1-sulfonate (21c). Yield (81%). 1H NMR (400 MHz, DMSO- d_6) δ 7.68–7.42 (m, 2H), 6.06 (s, 1H), 5.41 (d, $J = 6.3$ Hz, 1H), 5.24 (d, $J = 5.9$ Hz, 1H), 5.13 (s, 2H), 4.36 (d, $J = 7.2$ Hz, 1H), 4.01–3.89 (m, 1H), 3.48–3.41 (m, 3H), 2.20–2.04 (m, 3H), 1.63–1.33 (m, 4H), 0.89–0.78 (m, 6H). HRMS m/z : $[M + Na]^+$ calculated for $C_{21}H_{25}F_3N_3Na_2O_8S$ 620.1078; found 620.1069.

Sodium-(2S)-1-hydroxy-2-(((S)-4-methyl-2-(((perfluorophenyl)methoxy- d_2)carbonyl)amino)pentanamido)-3-(2-oxopyrrolidin-3-yl)propane-1-sulfonate (22c). Yield (89%). 1H NMR (400 MHz, DMSO- d_6) δ 7.67 (d, $J = 9.1$ Hz, 1H), 7.58 (s, 1H), 7.50 (d, $J = 8.8$ Hz, 1H), 5.12 (d, $J = 12.4$ Hz, 1H), 4.42–4.36 (m, 1H), 3.99–3.90 (m, 2H), 3.16–3.00 (m, 2H), 2.20–2.05 (m, 3H), 1.77 (s, 1H), 1.62–1.50 (m, 2H), 1.47–1.37 (m, 2H), 0.88–0.78 (m, 6H). HRMS m/z : $[M + Na]^+$ calculated for $C_{21}H_{23}D_2F_3N_3Na_2O_8S$ 622.1204; found 622.1193.

Sodium-(2S)-1-hydroxy-2-(((2S)-4-methyl-2-(((1-phenylbutoxy)carbonyl)amino)pentanamido)-3-(((S)-2-oxopyrrolidin-3-yl)propane-1-sulfonate (23c). Yield (63%). 1H NMR (400 MHz, DMSO- d_6) δ 7.60 (d, $J = 9.8$ Hz, 1H), 7.47 (d, $J = 5.0$ Hz, 1H), 7.41 (d, $J = 7.4$ Hz, 1H), 7.38–7.22 (m, 5H), 5.54 (t, $J = 6.6, 6.6$ Hz, 1H), 5.37–5.25 (m, 1H), 4.12–3.78 (m, 2H), 3.17–2.95 (m, 2H), 2.31–1.88 (m, 3H), 1.85–1.38 (m, 4H), 1.36–1.18 (m, 2H), 0.93–0.82 (m,

10H), 0.79–0.70 (m, 2H). HRMS m/z : $[M + Na]^+$ calculated for $C_{24}H_{36}N_3Na_2O_8S$ 572.2019; found 572.2005.

Sodium-(2S)-2-((2S)-2-(((1,2-diphenylethoxy)carbonyl)amino)-4-methylpentanamido)-1-hydroxy-3-((S)-2-oxopyrrolidin-3-yl)propane-1-sulfonate (24c). Yield (69%). 1H NMR (400 MHz, DMSO- d_6) δ 7.69–7.36 (m, 2H), 7.36–7.07 (m, 1H), 5.82–5.71 (m, 1H), 5.59–5.32 (m, 1H), 4.15–3.81 (m, 2H), 3.18–2.76 (m, 4H), 2.32–1.72 (m, 4H), 1.71–1.30 (m, 4H), 0.90–0.60 (m, 6H). HRMS m/z : $[M + Na]^+$ calculated for $C_{28}H_{36}N_3Na_2O_8S$ 620.2019; found 620.2007.

Biochemical Studies. Enzyme Assays and Inhibition Studies. Cloning and Expression of the 3CLpro of SARS-CoV-2 and FRET Enzyme Assays. The codon-optimized cDNA of full-length 3CLpro of SARS-CoV-2 (GenBank number MN908947.3) fused with sequences encoding six histidines at the N-terminal was synthesized by Integrated DNA (Coralville, IA). The synthesized gene was subcloned into the pET-28a(+) vector. The expression and purification of SARS-CoV-2 3CLpro were conducted following a standard procedure described previously.¹⁹ Briefly, a stock solution of an inhibitor was prepared in dimethyl sulfoxide (DMSO) and diluted in assay buffer composed of 20 mM 4-(2-hydroxyethyl)-1-piperazineethanesulfonic acid (HEPES) buffer, pH 8, containing NaCl (200 mM), ethylenediaminetetraacetic acid (EDTA) (0.4 mM), glycerol (60%), and 6 mM dithiothreitol (DTT). The SARS-CoV-2 3CLpro was mixed with serial dilutions of compound or with DMSO in 25 μ L of assay buffer and incubated at 37 °C for 1 h, followed by the addition of 25 μ L of assay buffer containing substrate (FAM-SAVLQ/SG-QXLS20, AnaSpec, Fremont, CA). The substrate was derived from the cleavage sites on the viral polyproteins of SARS-CoV. Fluorescence readings were obtained using an excitation wavelength of 480 nm and an emission wavelength of 520 nm on a fluorescence microplate reader (FLx800; Biotec, Winooski, VT) 1 h following the addition of substrate. Relative fluorescence units (RFUs) were determined by subtracting background values (substrate-containing well without protease) from the raw fluorescence values, as described previously. The dose-dependent FRET inhibition curves were fitted with a variable slope using GraphPad Prism software (GraphPad, La Jolla, CA) to determine the IC_{50} values of the compounds. The expression and purification of the 3CLpro of MERS-CoV, as well as the FRET enzyme assays, were performed as described previously.^{19–21,33}

Cell-Based Assay to Screen SARS-CoV-2 3CLpro Inhibitors. Two plasmids, pR-SARS-CoV-2 3CLpro and pGlo-VRLQS, were used for the system (Figure 1/panel A). First, the open reading frame of SARS-CoV-2 3CLpro was cloned to the reverse genetics system of PRRSV with GFP³⁵ and designated as pR-SARS-CoV-2 3CLpro. The GFP gene was replaced with SARS-CoV-2 3CLpro gene with *AflIII* and *MluI* enzyme sites. As a negative control, the inactive form of the 3CLpro was introduced to pR-SARS-CoV-2 3CLpro by the mutagenesis, and resulting plasmid was designated as pR-SARS-CoV-2 3CLpro C145A. Second, the plasmid was utilized with the pGloSensor caspase-3/7 biosensor (Promega, Madison, WI), which contains a caspase-3/7 cleavage site engineered in the Firefly luciferase gene. This plasmid also contains intact Renilla luciferase gene as an expression control. After transfection of pGloSensor caspase-3/7 to cells, the Firefly luciferase is expressed as an inactive form, and in the presence of caspase-3/7, it is activated after the cleavage. The caspase-3/7 cleavage site in this plasmid was replaced with CoV 3CLpro recognition sequences, VRLQS, designated as pGlo-VRLQS.³⁴ As a result, the expressed inactive luciferase is activated by the cleavage with CoV 3CLpro in the cells (Figure 1/panel A). HEK293T cells were used for transfection and the compound screening (Figure 1/panel B). One day old HEK293T cells in 48-well plates were cotransfected with two plasmids, pR-SARS-CoV-2 3CLpro and pGlo-VRLQS, or pR-SARS-CoV-2 3CLpro C145A (serves as a negative control) and pGlo-VRLQS. Following morning, the medium containing Mock-DMSO or serial concentrations of each compound were replaced to the transfected cells and incubated at 37 °C for 6 h. Cell lysates were prepared for testing the levels of Firefly and Renilla luciferases (Dual Luciferase assay kit, Promega) in a luminometer (Promega). The expression levels of Firefly luciferase were normalized with Renilla luciferase levels. The transfection of pR-

SARS-CoV-2 3CLpro C145A and pGlo-VRLQS resulted in minimal levels of Firefly luciferase, and this was applied to adjust all Firefly expression levels. The inhibition curve (Figure 1/panel C) for each compound was prepared, and the 50% effective concentration (EC_{50}) values were determined by GraphPad Prism software using a variable slope (GraphPad, La Jolla, CA). Compounds 4c and 15c were selected and examined for the antiviral effects with live SARS-CoV-2 in Vero E6 cells as described before,³³ and the EC_{50} was calculated by the same method described above. A known SARS-CoV-2 3CLpro inhibitor, GC376, was used as the positive control in each experiment. When GC376 and the selected compounds were examined if they inhibited the replication of PRRSV, none of them resulted in the reduction of viral replication.

Nonspecific Cytotoxic Effects/In Vitro Cytotoxicity. HEK293T cells grown in 96-well plates were incubated with various concentrations (1–100 μ M) of each compound for 72 h. Cell cytotoxicity was measured by a CytoTox 96 nonradioactive cytotoxicity assay kit (Promega), and the CC_{50} values were calculated using a variable slope by GraphPad Prism software.

X-ray Crystallographic Studies. Crystallization and Data Collection. Purified SARS-CoV-2 3CLpro¹⁹ in 100 mM NaCl, 20 mM Tris pH 8.0 was concentrated to 9.6 mg/mL (0.28 mM) for crystallization screening. All crystallization experiments were set up using an NT8 drop-setting robot (Formulatrix Inc.) and UVXPO MRC (Molecular Dimensions) sitting drop vapor diffusion plates at 18 °C. One hundred nanoliters of protein and 100 nL of crystallization solution were dispensed and equilibrated against 50 μ L of the latter. A stock solution of 100 mM compound was prepared in DMSO, and the SARS-CoV-2 3CLpro:compound complex was prepared by mixing 1 μ L of the ligand (2 mM) with 49 μ L (0.28 mM) of SARS2 3CLpro and incubating on ice for 1 h. Crystals were obtained in 1–2 days from various conditions for the following complexes: **8b**: Proplex HT screen (Molecular Dimensions) condition F7 (0.5 M ammonium sulfate, 100 mM MES pH 6.5); **12b**, **13c**, **14c**, and **21c**: Index HT screen (Hampton Research) condition D10 (20% (w/v) poly(ethylene glycol) (PEG) 5000 monomethyl ether (MME), 100 mM Bis–Tris pH 6.5); **19b** and **20b**: Proplex HT screen (Rigaku Reagents) condition C5 (20% (w/v) PEG 4000, 100 mM Tris pH 8.0); **1c**: Index HT screen (Hampton Research) condition F2 (20% (w/v) PEG 2000 MME, 100 mM Tris pH 8.5, 200 mM Trimethylamine N-oxide dihydrate); **3c**: Index HT screen (Hampton Research) condition F5 (17% (w/v) PEG 10 000, 100 mM Bis–Tris pH 5.5, 100 mM ammonium acetate); **5c**: Index HT screen (Hampton Research) condition F1 (10% (w/v) PEG 3350, 100 mM Hepes pH 7.5, 200 L-proline); and **17c** and **18c**: Index HT screen (Rigaku Reagents) condition H11 (30% (w/v) PEG 2000 MME, 100 mM potassium thiocyanate). Samples were transferred to a fresh drop composed of 80% crystallization solution and 20% (v/v) PEG 200 and stored in liquid nitrogen. Crystals of SARS-CoV-2 3CLpro with **8b** were transferred to a cryoprotectant solution containing 80% crystallant and 20% (v/v) glycerol prior to freezing. X-ray diffraction data were collected at the Advanced Photon Source beamline except for the SARS-CoV-2 3CLpro complex with **14c**, which were collected at the National Synchrotron Light Source II (NSLS-II) AMX beamline 17-ID-1. All diffraction data were collected using a Dectris Eiger2 X 9M pixel array detector.

Structure Solution and Refinement. Intensities were integrated using XDS^{40,41} via Autoproc,⁴² and the Laue class analysis and data scaling were performed with Aimless.⁴³ Structure solution was conducted by molecular replacement with Phaser⁴⁴ using a previously determined structure of SARS2 3CLpro (PDB 6XMK¹⁹) as the search model. Structure refinement and manual model building were conducted with Phenix⁴⁵ and Coot,⁴⁶ respectively. Disordered side chains were truncated to the point for which electron density could be observed. Structure validation was conducted with Molprobity,⁴⁷ and figures were prepared using the CCP4MG⁴⁸ package. Crystallographic data are provided in Table S1.^{49–53}

■ ASSOCIATED CONTENT

SI Supporting Information

The Supporting Information is available free of charge at <https://pubs.acs.org/doi/10.1021/acs.jmedchem.1c01037>.

Binding modes of **19b** and **20b** with SARS-CoV-2 3CLpro associated with subunit A and subunit B, surface representation showing the orientation of **19b** on the SARS-CoV-2 3CLpro surface, crystallographic data for SARS-CoV-2 3CLpro inhibitor complexes, and absolute qNMR data (PDF)

Molecular formula strings—SMILES codes (CSV)

Accession Codes

Coordinates and structure factors for the following SARS2 3CLpro complexes with inhibitors were deposited to the Worldwide Protein Databank (wwPDB) with the accession codes: **8b** (7LZT), **12b** (7LZU), **19b** (7LZV), **20b** (7LZW), **1c** (7LZX), **3c** (7LZY), **5c** (7LZZ), **13c** (7M00), **14c** (7M01), **17c** (7M02), **18c** (7M03), and **21c** (7M04). The authors will release the atomic coordinates upon article publication.

■ AUTHOR INFORMATION

Corresponding Authors

Yunjeong Kim – Department of Diagnostic Medicine & Pathobiology, College of Veterinary Medicine, Kansas State University, Manhattan, Kansas 66506, United States; Phone: 785-532-4616; Email: ykim@ksu.edu

William C. Groutas – Department of Chemistry, Wichita State University, Wichita, Kansas 67260, United States; orcid.org/0000-0001-5248-7912; Phone: 316-978-7374; Email: bill.groutas@wichita.edu

Kyeong-Ok Chang – Department of Diagnostic Medicine & Pathobiology, College of Veterinary Medicine, Kansas State University, Manhattan, Kansas 66506, United States; Phone: 785-532-3849; Email: kchang@vet.ksu.edu

Authors

Chamandi S. Dampalla – Department of Chemistry, Wichita State University, Wichita, Kansas 67260, United States; orcid.org/0000-0002-8199-2376

Athri D. Rathnayake – Department of Chemistry, Wichita State University, Wichita, Kansas 67260, United States; orcid.org/0000-0003-2588-7624

Krishani Dinali Perera – Department of Diagnostic Medicine & Pathobiology, College of Veterinary Medicine, Kansas State University, Manhattan, Kansas 66506, United States; orcid.org/0000-0002-3778-4975

Abdul-Rahman M. Jesri – Department of Chemistry, Wichita State University, Wichita, Kansas 67260, United States

Harry Nhat Nguyen – Department of Chemistry, Wichita State University, Wichita, Kansas 67260, United States

Matthew J. Miller – Department of Chemistry, Wichita State University, Wichita, Kansas 67260, United States

Hayden A. Thurman – Department of Chemistry, Wichita State University, Wichita, Kansas 67260, United States

Jian Zheng – Department of Microbiology and Immunology, University of Iowa, Iowa City, Iowa 52242, United States

Maithri M. Kashipathy – Protein Structure Laboratory, The University of Kansas, Lawrence, Kansas 66047, United States

Kevin P. Battaile – NYX, New York Structural Biology Center, Upton, New York 11973, United States; orcid.org/0000-0003-0833-3259

Scott Lovell – Protein Structure Laboratory, The University of Kansas, Lawrence, Kansas 66047, United States

Stanley Perlman – Department of Microbiology and Immunology, University of Iowa, Iowa City, Iowa 52242, United States

Complete contact information is available at:

<https://pubs.acs.org/10.1021/acs.jmedchem.1c01037>

Author Contributions

*C.S.D. and A.D.R. contributed equally to this work.

Notes

The authors declare no competing financial interest.

■ ACKNOWLEDGMENTS

This research was supported, in part, by grants from the National Institutes of Health (NIH) (R01 AI109039 to K.-O.C.). Use of the University of Kansas Protein Structure Laboratory was supported by a grant from the National Institute of General Medical Sciences (P30GM110761) of the NIH. Support for the NMR instrumentation was provided by NIH Shared Instrumentation Grant # S10RR024664 and NSF Major Research Instrumentation Award #1625923. Use of the IMCA-CAT beamline 17-ID at the Advanced Photon Source was supported by the companies of the Industrial Macromolecular Crystallography Association through a contract with Hauptman-Woodward Medical Research Institute. Use of the Advanced Photon Source was supported by the U.S. Department of Energy, Office of Science, Office of Basic Energy Sciences under contract no. DE-AC02-06CH11357. This research used the AMX beamline of the National Synchrotron Light Source II, a U.S. Department of Energy (DOE) Office of Science User Facility operated for the DOE Office of Science by Brookhaven National Laboratory under Contract No. DE-SC0012704. The Center for Biomolecular Structure (CBMS) was primarily supported by the National Institutes of Health, the National Institute of General Medical Sciences (NIGMS) through a Center Core P30 Grant (P30GM133893), and the DOE Office of Biological and Environmental Research (KP1605010).

■ ABBREVIATIONS USED

CC₅₀, 50% cytotoxic concentration in cell-based assays; CDI, carbonyl diimidazole; CPE, cytopathic effects; DMSO, dimethyl sulfoxide; DMP, Dess–Martin periodinane; DSC, *N,N'*-disuccinimidyl carbonate; DTT, dithiothreitol; EC₅₀, the 50% effective concentration in cell culture; GESAMT, general efficient structural alignment of macromolecular targets; IC₅₀, the 50% inhibitory concentration in the enzyme assay; MME, monomethyl ether; MNV, murine norovirus; MOI, multiplicity of infection; ORF, open reading frame; PK, pharmacokinetics; RMSD, root-mean-square deviation; TCID₅₀, the 50% tissue culture infectious dose; TEA, triethyl amine; XDS, X-ray detector software

■ REFERENCES

- (1) Wu, F.; Zhao, S.; Yu, B.; Chen, Y.-M.; Wang, W.; Song, Z.-G.; Hu, Y.; Tao, Z.-W.; Tian, J.-H.; Pei, Y.-Y.; Yuan, M.-L.; Zhang, Y.-L.; Dai, F.-H.; Liu, Y.; Wang, Q.-M.; Zheng, J.-J.; Xu, L.; Holmes, E. C.; Zhang, Y.-Z. A new coronavirus associated with human respiratory disease in China. *Nature* **2020**, *579*, 265–269.
- (2) Fontanet, A.; Autran, B.; Lina, B.; Kieny, M. P.; Abdool Karim, S. S.; Sridhar, D. SARS-CoV-2 variants and ending the COVID-19 pandemic. *Lancet* **2021**, *397*, 952–954.

- (3) Yurkovetskiy, L.; Wang, X.; Pascal, K. E.; Tomkins-Tinch, C.; Nyalile, T. P.; Wang, Y.; Baum, A.; Diehl, W. E.; Dauphin, A.; Carbone, C.; Veinotte, K.; Egri, S. B.; Schaffner, S. F.; Lemieux, J.; Munro, J. B.; Rafique, A.; Barve, A.; Sabeti, P. C.; Kyratsous, C. A.; Dudkina, N. V.; Shen, K.; Luban, J. Structural and functional analysis of the D614G SARS-CoV-2 spike protein variant. *Cell* **2020**, *183*, 739–751.
- (4) Wu, D.; Koganti, R.; Lambe, U. P.; Yadavalli, T.; Nandi, S. S.; Shukla, D. Vaccines and therapies in development for SARS-CoV-2 infections. *J. Clin. Med.* **2020**, *9*, No. 1885.
- (5) Wang, C.; Li, W.; Drabek, D.; Okba, N. M. A.; Haperen, R. V.; Osterhaus, A. D. M. E.; Kuppeveld, F. J. M. V.; Haagmans, B. L.; Grosveld, F.; Bosch, B.-J. A human monoclonal antibody blocking SARS-CoV-2. *Nat. Commun.* **2020**, *11*, No. 2251.
- (6) Ghosh, A. K.; Brindisi, M.; Shahabi, D.; Chapman, M. E.; Mesecar, A. D. Drug development and medicinal chemistry efforts toward SARS-Coronavirus and Covid-19 therapeutics. *Chem. Med. Chem.* **2020**, *15*, 907–932.
- (7) Gil, C.; Ginex, T.; Maestro, I.; Nozal, V.; Barrado-Gil, L.; Cuesta-Geijo, M. A.; Urquiza, J.; Ramirez, D.; Alonso, C.; Campillo, N. E.; Martinez, A. COVID-19: Drug targets and potential treatments. *J. Med. Chem.* **2020**, *63*, 12359–12386.
- (8) Sharma, A.; Tiwari, S.; Deb, M. K.; Marty, J. L. Severe Acute Respiratory Syndrome Coronavirus-2 (SARS-CoV-2): A global pandemic and treatments strategies. *Int. J. Antimicrob. Agents* **2020**, *56*, No. 106054.
- (9) Cannalire, R.; Cerchia, C.; Beccari, A. R.; Di Leva, F. S.; Summa, V. Targeting SARS-CoV-2 proteases and polymerase for COVID-19 treatment: State of the art and future opportunities. *J. Med. Chem.* **2020**, No. 01140.
- (10) Ullrich, S.; Nitsche, C. The SARS-CoV-2 main protease as drug target. *Bioorg. Med. Chem. Lett.* **2020**, *30*, No. 127377.
- (11) Konwar, M.; Sarma, D. Advances in developing small molecule SARS 3CLpro inhibitors as potential remedy for Corona Virus infection. *Tetrahedron* **2021**, *77*, No. 131761.
- (12) He, J.; Hu, L.; Huang, X.; Wang, C.; Zhang, Z.; Wang, Y.; Zhang, D.; Ye, W. Potential of coronavirus 3C-like protease inhibitors for the development of new anti-SARS-CoV-2 drugs: Insights from structures of protease and inhibitors. *Int. J. Antimicrob. Agents* **2020**, *56*, No. 106055.
- (13) Jin, Z.; Du, X.; Xu, Y.; Deng, Y.; Liu, M.; Zhao, Y.; Zhang, B.; Li, X.; Zhang, L.; Peng, C.; Duan, Y.; Yu, J.; Wang, L.; Yang, K.; Liu, F.; Jiang, R.; Yang, X.; You, T.; Liu, X.; Yang, X.; Bai, F.; Liu, H.; Liu, X.; Guddat, L. W.; Xu, W.; Xiao, G.; Qin, C.; Shi, Z.; Jiang, H.; Rao, Z.; Yang, H. Structure of M pro from SARS-CoV-2 and discovery of its inhibitors. *Nature* **2020**, *582*, 289–293.
- (14) Zhang, L.; Lin, D.; Sun, X.; Curth, U.; Drosten, C.; Sauerhering, L.; Becker, S.; Rox, K.; Hilgenfeld, R. Crystal structure of SARS-CoV-2 main protease provides a basis for design of improved α -ketoamide inhibitors. *Science* **2020**, *368*, 409–412.
- (15) Dai, W.; Zhang, B.; Jiang, X.-M.; Su, H.; Li, J.; Zhao, Y.; Xie, X.; Jin, Z.; Peng, J.; Liu, F.; Li, C.; Li, Y.; Bai, F.; Wang, H.; Cheng, X.; Cen, X.; Hu, S.; Yang, X.; Wang, J.; Liu, X.; Xiao, G.; Jiang, H.; Rao, Z.; Zhang, L.-K.; Xu, Y.; Yang, H.; Liu, H. Structure-based design of antiviral drug candidates targeting the SARS-CoV-2 main protease. *Science* **2020**, *368*, 1331–1335.
- (16) Qiao, J.; Li, Y.-S.; Zeng, R.; Liu, F.-L.; Luo, R.-H.; Huang, C.; Wang, Y.-F.; Zhang, J.; Quan, B.; Shen, C.; Mao, X.; Liu, X.; Sun, W.; Yang, W.; Ni, X.; Wang, K.; Xu, L.; Duan, Z.-L.; Zou, Q.-C.; Zhang, H.-L.; Qu, W.; Long, Y.-H.-P.; Li, M.-H.; Yang, R.-C.; Liu, X.; You, J.; Zhou, Y.; Yao, R.; Li, W.-P.; Liu, J.-M.; Chen, P.; Liu, Y.; Lin, G.-F.; Yang, X.; Zou, J.; Li, L.; Hu, Y.; Lu, G.-W.; Li, W.-M.; Wei, Y.-Q.; Zheng, Y.-T.; Lei, J.; Yang, S. SARS-CoV-2 M^{pro} inhibitors with antiviral activity in a transgenic mouse model. *Science* **2021**, *371*, 1374–1378.
- (17) Schechter, I. Reprint of “on the size of the active site in proteases. I. Papain”. *Biochem. Biophys. Res. Commun.* **2012**, *425*, 497–502. The nomenclature used is that of Schechter, I. and Berger, A., where the residues on the N-terminus side of the peptide bond that is cleaved are designated as P₁-P_n and those on the C-terminus side are designated P₁-P₁'. The corresponding active site subsites are designated S₁-S_n and S₁-S₁'.
- (18) Kreutzer, A. G.; Krumberger, M.; Parrocha, C. M. T.; Morris, M. A.; Guaglianone, G.; Nowick, J. S. Structure-Based Design of a Cyclic Peptide Inhibitor of the SARS-CoV-2 Main Protease. bioRxiv [online early access]. DOI: 10.1101/2020.08.03.234872. Published Online: Aug 03, 2020. <https://doi.org/10.1021/acs.jmedchem.0c01140> (accessed Aug 03, 2020).
- (19) Rathnayake, A. D.; Zheng, J.; Kim, Y.; Perera, K. D.; Mackin, S.; Meyerholz, D. K.; Kashipathy, M. M.; Battaile, K. P.; Lovell, S.; Perlman, S. 3C-like protease inhibitors block coronavirus replication in vitro and improve survival in MERS-CoV-infected mice. *Sci. Transl. Med.* **2020**, *12*, No. eabc5332.
- (20) Galasiti Kankanamalage, A. C.; Kim, Y.; Damalanka, V. C.; Rathnayake, A. D.; Fehr, A. R.; Mehzabeen, N.; Battaile, K. P.; Lovell, S.; Lushington, G. H.; Perlman, S.; Chang, K. O.; Groutas, W. C. Structure-guided design of potent and permeable inhibitors of MERS coronavirus 3CL protease that utilize a piperidine moiety as a novel design element. *Eur. J. Med. Chem.* **2018**, *150*, 334–346.
- (21) Kim, Y.; Lovell, S.; Tiew, K.-C.; Mandadapu, S. R.; Alliston, K. R.; Battaile, K. P.; Groutas, W. C.; Chang, K.-O. Broad-spectrum antivirals against 3C or 3C-like proteases of picornaviruses, noroviruses, and coronaviruses. *J. Virol.* **2012**, *86*, 11754–11762.
- (22) Kim, Y.; Liu, H.; Galasiti Kankanamalage, A. C.; Weerasekara, S.; Hua, D. H.; Groutas, W. C.; Chang, K.-O.; Pedersen, N. C. Reversal of the progression of fatal coronavirus infection in cats by a broad-spectrum coronavirus protease inhibitor. *PLoS Pathog.* **2016**, *12*, No. e1005531.
- (23) Pedersen, N. C.; Kim, Y.; Liu, H.; Galasiti Kankanamalage, A. C.; Eckstrand, C.; Groutas, W. C.; Bannasch, M.; Meadows, J. M.; Chang, K.-O. Efficacy of a 3C-like protease inhibitor in treating various forms of acquired feline infectious peritonitis. *J. Feline Med. Surg.* **2018**, *20*, 378–392.
- (24) Pennington, L. D.; Aquila, B. M.; Choi, Y.; Valiulin, R. A.; Muegge, I. Positional analog scanning: an effective strategy for multiparameter optimization in drug design. *J. Med. Chem.* **2020**, *63*, 8956–8976.
- (25) Vulpetti, A.; Hommel, U.; Landrum, G.; Lewis, R.; Dalvit, C. Design and NMR-based screening of LEF, a library of chemical fragments with different local environments of fluorine. *J. Am. Chem. Soc.* **2009**, *131*, 12949–12959.
- (26) Piralì, T.; Serafini, M.; Cargini, S.; Genazzani, A. A. Applications of deuterium in medicinal chemistry. *J. Med. Chem.* **2019**, *62*, 5276–5297.
- (27) Timmins, G. S. Deuterated drugs: updates and obviousness analysis. *Expert Opin. Ther. Pat.* **2017**, *27*, 1353–1361.
- (28) Liu, J. F.; et al. A decade of deuteration in medicinal chemistry. *Ann. Rep. Med. Chem.* **2017**, *50*, 519–542.
- (29) Kim, H.-O.; Kahn, M. The synthesis of aminoazole analogs of lysine and arginine: the Mitsunobu reaction with lysinol and arginol. *Synlett* **1999**, *8*, 1239–1240.
- (30) Maity, P.; Gujjar, M.; Vellingiri, R.; Lakshminarasimhan, T.; DelMonte, A. J.; Young, I. S.; Eastgate, M. D.; Vaidyanathan, R. Cerium(III) chloride-mediated stereoselective reduction of a 4-substituted cyclohexanone using NaBH₄. *Org. Process Res. Dev.* **2019**, *23*, 2754–2757.
- (31) Ghosh, A. K.; Duong, T. T.; McKee, S. P.; Thompson, W. J. N, N'-Disuccinimidyl carbonate: A useful reagent for alkoxy-carbonylation of amines. *Tetrahedron Lett.* **1992**, *33*, 2781–2784.
- (32) Kjell, D. P.; Slattery, B. J.; Semo, M. J. A novel, nonaqueous method for regeneration of aldehydes from bisulfite adducts. *J. Org. Chem.* **1999**, *64*, 5722–5724.
- (33) Dampalla, C. S.; Zheng, J.; Perera, K. D.; Wong, L.-Y. R.; Meyerholz, D. K.; Nguyen, H. N.; Kashipathy, M. M.; Battaile, K. P.; Lovell, S.; Kim, Y.; Perlman, S.; Groutas, W. C.; Chang, K.-O. Post-infection treatment with a protease inhibitor increases survival of mice with a fatal SARS-CoV-2 infection. *Proc. Natl. Acad. Sci. U.S.A.* **2021**, *118*, No. e2101555118.

- (34) O'Brien, A.; Chen, D.-Y.; Hackbart, M.; Close, B. J.; O'Brien, T. E.; Saeed, M.; Baker, S. C. Detecting SARS-CoV-2 3CLpro expression and activity using a polyclonal antiserum and a luciferase-based biosensor. *Virology* **2021**, *556*, 73–78.
- (35) Lawson, S. R.; Li, Y.; Patton, J. B.; Langenhorst, R. J.; Sun, Z.; Jiang, Z.; Christopher-Hennings, J.; Nelson, E. A.; Knudsen, D.; Fang, Y.; Chang, K.-O. Interleukin-1 β expression by a recombinant PRRSV enhanced viral specific host immunity. *Virus Res.* **2012**, *163*, 461–468.
- (36) Cao, W.; Cho, C.-C. D.; Geng, Z. Z.; Ma, X. R.; Allen, R.; Shaabani, N.; Vatansever, E. C.; Alugubelli, Y. R.; Ellenburg, W. H.; Yang, K.; Qiao, Y.; Ji, H.; Xu, S.; Liu, W. R. Cellular Activity of SARS-CoV-2 Main Protease Inhibitors Reveal Their Unique Characteristics. *bioRxiv* [online early access]. DOI: 10.1101/2021.06.08.447613. Published Online: June 9, 2021. <https://doi.org/10.1101/2021.06.08.447613> (accessed Aug 3, 2021).
- (37) Resnick, S. J.; Iketani, S.; Hong, S. J.; Zask, A.; Liu, H.; Kim, S.; Melore, S.; Nair, M. S.; Huang, Y.; Tay, N. E. S.; Rovis, T.; Yang, H. W.; Stockwell, B. R.; Ho, D. D.; Chavez, A. A Simplified Cell-Based Assay to Identify Coronavirus 3CL Protease Inhibitors. *bioRxiv* [online early access]. DOI: 10.1101/2020.08.29.272864. Published Online: Aug 29, 2020. <https://doi.org/10.1101/2020.08.29.272864> (accessed Aug 3, 2021).
- (38) Talele, T. T. Natural products-inspired use of the *gem*-dimethyl group in medicinal chemistry. *J. Med. Chem.* **2018**, *61*, 2166–2210.
- (39) Pennington, L. D.; Moustakas, D. T. The necessary nitrogen atom: a versatile high-impact design element for multiparameter optimization. *J. Med. Chem.* **2017**, *60*, 3552–3579.
- (40) Kabsch, W. Automatic indexing of rotation diffraction patterns. *J. Appl. Crystallogr.* **1988**, *21*, 67–72.
- (41) Kabsch, W. XDS. *Acta Crystallogr., Sect. D: Biol. Crystallogr.* **2010**, *66*, 125–132.
- (42) Vonrhein, C.; Flensburg, C.; Keller, P.; Sharff, A.; Smart, O.; Paciorek, W.; Womack, T.; Bricogne, G. Data processing and analysis with the autoPROC toolbox. *Acta Crystallogr., Sect. D: Biol. Crystallogr.* **2011**, *67*, 293–302.
- (43) Evans, P. R. An introduction to data reduction: space-group determination, scaling and intensity statistics. *Acta Crystallogr., Sect. D: Biol. Crystallogr.* **2011**, *67*, 282–292.
- (44) McCoy, A. J.; Grosse-Kunstleve, R. W.; Adams, P. D.; Winn, M. D.; Storoni, L. C.; Read, R. J. Phaser crystallographic software. *J. Appl. Crystallogr.* **2007**, *40*, 658–674.
- (45) Adams, P. D.; Afonine, P. V.; Bunkóczi, G.; Chen, V. B.; Davis, I. W.; Echols, N.; Headd, J. J.; Hung, L.-W.; Kapral, G. J.; Grosse-Kunstleve, R. W. PHENIX: a comprehensive Python-based system for macromolecular structure solution. *Acta Crystallogr., Sect. D: Biol. Crystallogr.* **2010**, *66*, 213–221.
- (46) Emsley, P.; Lohkamp, B.; Scott, W. G.; Cowtan, K. Features and development of Coot. *Acta Crystallogr., Sect. D: Biol. Crystallogr.* **2010**, *66*, 486–501.
- (47) Chen, V. B.; Arendall, W. B.; Headd, J. J.; Keedy, D. A.; Immormino, R. M.; Kapral, G. J.; Murray, L. W.; Richardson, J. S.; Richardson, D. C. MolProbity: all-atom structure validation for macromolecular crystallography. *Acta Crystallogr., Sect. D: Biol. Crystallogr.* **2010**, *66*, 12–21.
- (48) Potterton, L.; McNicholas, S.; Krissinel, E.; Gruber, J.; Cowtan, K.; Emsley, P.; Murshudov, G. N.; Cohen, S.; Perrakis, A.; Noble, M. Developments in the CCP4 molecular-graphics project. *Acta Crystallogr., Sect. D: Biol. Crystallogr.* **2004**, *60*, 2288–2294.
- (49) Evans, P. Scaling and assessment of data quality. *Acta Crystallogr., Sect. D: Biol. Crystallogr.* **2006**, *62*, 72–82.
- (50) Diederichs, K.; Karplus, P. A. Improved R-factors for diffraction data analysis in macromolecular crystallography. *Nat. Struct. Biol.* **1997**, *4*, 269–275.
- (51) Weiss, M. S. Global indicators of X-ray data quality. *J. Appl. Crystallogr.* **2001**, *34*, 130–135.
- (52) Karplus, P. A.; Diederichs, K. Linking crystallographic model and data quality. *Science* **2012**, *336*, 1030–1033.
- (53) Evans, P. Biochemistry. Resolving some old problems in protein crystallography. *Science* **2012**, *336*, 986–987.
- (54) The purity of some of the aldehyde inhibitors ranged between 89–94% due to the facile epimerization of the aldehyde α -carbon upon storage (see [Supporting Information](#)).